UC Irvine
UC Irvine Electronic Theses and Dissertations

Title

Droplet-based Microfluidic Devices for Single-cell Analysis and Cell-pairing Applications

Permalink

Author

Luo, Xuhao

Publication Date

2023

Peer reviewed|Thesis/dissertation

UNIVERSITY OF CALIFORNIA, IRVINE

**Droplet-based Microfluidic Devices for
Single-cell Analysis and Cell-pairing Applications**

DISSERTATION

submitted in partial satisfaction of the requirements for the degree of

DOCTOR OF PHILOSOPHY

in BIOMEDICAL ENGINEERING

by

Xuhao Luo

Dissertation committee:
Professor Abraham P. Lee, Chair
Associate Professor Jered Haun
Associate Professor Elliot Hui

2023

DEDICATION

To

my parents, Jingxian Luo and Saiying Sun,

who have supported, believed, stood by, and brought out the very best in me

I would not be where I am without them

TABLE OF CONTENTS

LIST OF FIGURES

Page

Chapter 1:

Chapter 2:

Chapter 3:

Chapter 4:

ACKNOWLEDGEMENTS

Word cannot express my gratitude to the following people, without whom I would not have made it through my PhD journey. First and foremost, I would like to express my sincere gratitude to my advisor, Dr. Abraham Lee for his invaluable advice, continuous trust and support, and patience during my PhD study. Dr. Lee's aspiration and determination of advancing science continuously inspired me to push the boundary of existing microfluidic technology despite countless failed experiments. I appreciate the trust he has given me, which allowed me to freely explore various directions to address engineering challenges. His generous support and mentorship do not only have shaped me as a scientist but also an individual. This dissertation would not have been possible without his guidance.

Additionally, I would like to express my sincere gratitude to Dr. Elliot Hui and Dr. Jered Haun, who served as committee members on my qualifying exam and dissertation. Dr. Hui's experience in droplet microfluidics and integrated microfluidic logic has been a great resource for me while I was working on the droplet co-encapsulation project. Dr. Haun's research on microfluidic tissue dissociation for single cell analysis has inspired me to explore the biological applications for my project that involves microvortices in cell-laden droplets. Their insightful advises have helped me to tackle many research challenges throughout the years. I would like to extend my sincere thanks to my former collaborator, Dr. Michelle Digman and Dr. Francesco Palomba, who enabled the integration of the droplet microfluidic platform with the cutting-edge fluorescence life-time microscopy for downstream analysis. I appreciate their mentorship and patience on teaching me this advanced microscopy and imaging analysis techniques. We did not only have developed innovative microfluidic platforms for microscopy, but also friendship.

It was my honor to be a part of BioMiNT lab for my PhD career and work with all the lab members. Great thanks to Dr. Xuan Li, who trained me when I first joined the lab. Despite her busy full-time schedule at Takara, she continuously offered support and valuable advice on several of my projects. I would also like to thank Dr. Jui-Yi (Becky) Chen and Dr. Mohammad Aghaamoo for our countless number of inspiring discussions, which led to many interesting new ideas when I thought the project was impossible to solve. I would like to offer my special thanks to Braulio Cardenas Benitez. While I was overwhelmed with multiple projects, he collaborated with me to work on the droplet microvortices project with his expertise in fundamental fluid dynamics that led to an oral presentation in MicroTAS and patent. In addition, a thank you to all BioMiNT lab members: Dr. Reem Khojah, Ruoyu Jiang, Paul Byunghoon Yoo, Matthew Hsiu-Ping Yi, and Aida Taravat. Working with them has been a privilege, and they offered kind help in various aspects of my research.

I would like to express my heartfelt thank you to my cohorts and friends who accompanied me on this PhD journey, especially the difficult time during COVID period. My BME cohorts and friends: Yukai Huang, Chiahung Lee, Sungsik Chu, Pisrut Phummirat, and Songning Zhu. I am grateful to them for their feedback sessions and moral support that brighten my days.

Most importantly, none of this could have happened without my parents and family. My parents sacrifice their stable jobs to immigrate to the United States for the American Dream and provide better education for me. Being the first-generation college student in the family, their belief in me has kept me spirits and motivation high during this process. Wordsd cannot express my gratitude and love toward my parents, who constantly worked hard over the years to provide for my needs. I would also like to thank my uncle, Zhongxun Sun, who has been generously sharing his invaluable experiences in life and encouraging my pursuit of higher education. I am blessed to have many caring uncles, aunts, and cousins, who support me in various aspects of my life during my graduate school.

Xuhao Luo

EDUCATION

2018 – 2023	**Ph.D. Biomedical Engineering**
	University of California, Irvine
2018 – 2021	**M.S. Biomedical Engineering**
	University of California, Irvine
2011 – 2015	**B.S. Bioengineering**
	University of California, Berkeley

PROFESSIONAL EXPERIENCE

Apr. 2016 – Aug. 2018	**Research Associate**
	Complete Genomics, *San Jose, CA*
Jun. 2015 – Apr. 2016	**Research Associate**
	Scanadu, *Sunnyvale, CA*
Jan. 2015 – May 2015	**Software Engineer Intern**
	Spiral Devices, *Berkeley, CA*

TEACHING EXPERIENCE

Jan. 2023 – Mar. 2023	**Microfluidics & Lab-on-a-chip**
	Teaching Assistant BME 147 UC Irvine
	Dr. Abraham Lee
Sept. 2021 – Dec. 2021	**Genetics**
	Teaching Assistant Bio Sci 97 UC Irvine
	Dr. Rahul Warrior and Dr. Olivier Cinquin
Sept. 2020 – Jun. 2021	**Capstone Project**
	Graduate Student Mentor BME UC Irvine
	Dr. Abraham Lee
Aug. 2014 – May 2015	**Data Structures and Advanced Programming**
	Undergraduate Instructor Assistant CS 61B UC Berkeley
	Dr. Paul Hilfinger and Dr. Josh Hug

FIELD OF STUDY

Droplet Microfluidics, Single-cell Analysis, Sequencing

PUBLICATIONS / CONFERENCE PUBLICATIONS

1. **X. Luo**, B.C. Benitez, and A. Lee, "Effects of Single-cell Morphological Properties on their Translational and Rotational Dynamics inside Shear-induced Droplet Microvortices"
(In Preparation)

2. **X. Luo**, A. Lee, "Overcoming Double-*Poisson* Limitation for Co-encapsulation in Droplets through Hydrodynamic Close Packing of Cells", *Microfluidics and Nanofluidics*, 27 (3), 2023, doi.org/10.1007/s10404-022-02600-9

3. **X. Luo** and A. Lee, "Overcoming Double-Poisson Limitation for Co-encapsulation in Droplets through Hydrodynamic Close Packing of Cells", *26th International Conference on Miniaturized Systems for Chemistry and Life Sciences (MicroTAS 2022)*, Hangzhou, China, October 23-27, 2022 (Oral Presentation)

4. **X. Luo**, JY Chen, M. Ataei, A. Lee, "Microfluidic Compartmentalization Platforms for Single Cell Analysis", *Biosensors*, 12 (2), 2022, doi:10.3390/bios12020058

5. **X. Luo**, B. Cardenas-Benitez, F Palomba, M. Digman, A. Lee, "Hydrodynamically-Induced Droplet Microvortices for Cell Pairing Applications", *25th International Conference on Miniaturized Systems for Chemistry and Life Sciences (MicroTAS 2021)*, Palm Spring, California, USA, October 10-14, 2021 (Oral Presentation)

6. F. Palomba, M. Digman, **X. Luo**, A.P. Lee, "NADH Autofluorescence Phasor Flim for the Metabolic Characterization of T cell and Leukemia Cell in a Droplet", *Biophysical Journal,* 120 (3), 359a, 2021

7. N. Gulbahce*, M. J. Magbanua*, R. Chin, M. R. Agarwal, **X. Luo**, J. Liu, D. Hayden, Q. Mao, S. Ciotlos, Z. Li, Y. Chen, X. Chen, Y. Li, R. Zhang, K. Lee, R. Tearle, E. Park, S. Drmanac, H. S. Rugo, J. Park, R. Drmanac, & B. A. Peters, "Quantitative whole genome sequencing of circulating tumor cells enables personalized combination therapy of metastatic cancer", *Cancer Research*, 2017, Aug 15; 77 (16): 4530-4541. doi:10.1158/0008-5472.CAN-17-0688

PATENTS

1. **X. Luo**, B. Cardenas-Benitez, A. Lee, "Hydrodynamically-Induced Droplet Microvortices for Modulating Cell Dynamics" (Provisional Patent Filed 2022)

2. A.P. Lee, G. Kamalakshakurup, M. Aghaamoo, X. Li, G. Lin, **X. Luo**, M. Ataei, M. Digman, F. Palomba, "High-efficiency Particle Encapsulation in Droplets with Particle Spacing and Downstream Droplet Sorting", *US Patent App.* 16/707,560, 2020

ABSTRACT OF THE DISSERTATION

Droplet-based Microfluidic Platform for Single-cell and Cell Pairing Applications

by

Xuhao Luo

Doctor of Philosophy in Biomedical Engineering

University of California, Irvine, 2023

Professor Abraham Lee, Chair

Droplet microfluidics has become an indispensable technology to encapsulate cells of interest in a monodispersed aqueous compartment for single-cell analysis. In addition, the confinement of cells in picoliter droplets offers high-throughput, single-cell resolution, and high signal-to-noise ratio for various cellular assays that unmasks cellular heterogeneity from a bulk population. Particularly, co-encapsulation of two distinct cells in a droplet is critically important for studying cell–cell interaction, transcriptomics, genomics, antibody, and drug screening. However, the co-encapsulation of one type A cell and one type B cell per single droplet, termed 1–1–1 encapsulation, has been dictated by double *Poisson* distribution due to the intrinsic random dispersion of cells, which yields mostly empty droplets and only up to 13.5% of droplets under optimal conditions. Such low 1–1–1 encapsulation efficiency makes it impractical for biological analyses at scale involving low cell concentrations or a large number of variables. Here, we demonstrate a passive co-encapsulation microfluidic device that leverages close packing of cells by hydrodynamic draining to overcome the double *Poisson* limitation. The results suggest a significant improvement of the 1–1–1

encapsulation efficiency by over two-fold compared to the double *Poisson* model. The enhanced encapsulation efficiency of this platform demonstrates great potential for a high-throughput, versatile, and simple platform for cell–cell interaction studies within a confined microenvironment.

In addition, we present a microfluidic droplet trapping array capable of modulating the translational and rotational dynamics of trapped cells inside the droplets by means of shear-induced microvortices driven by external fluidic control. Using this platform, we demonstrate that droplet microvortices are sensitive to particle/cell size to droplet ratios, cell compliance, and the external phase fluid velocity. We further analyzed the hydrodynamic forces experienced by particles through theoretical and numerical simulations to better understand the effects of different physical variables on droplet recirculation dynamics. Our experimental and theoretical results provide insights into the fluidic conditions that lead to translational or rotational dynamics inside trapped droplets, and could enable future uses for the characterization of single-cell biophysical properties.

CHAPTER 1: INTRODUCTION AND BACKGROUND

1.1   Microfluidic Compartmentalization Platforms for Single Cell Analysis

Cell, as an indivisible unit of life, is the basic building block of all living organisms. Each individual cell provides a crucial basic structure and biological function, as well as the interplay between collective cells in response to perturbation [1, 2]. Conventional cell-based assays are often used to further categorize into different types according to their morphological, functional, and other phenotypic characteristics [3, 4]. This population-level cellular analysis plays an essential role in our understanding of pathogenesis and studying cellular mechanisms. However, many conventional cell-based assays yield ensemble measurements from a population of cells, with an assumption that an averaged result is representative of a typical individual cell within a population. This generalization can often lead to misleading interpretation, given the abundance of evidence that has demonstrated cellular heterogeneity within a clonal population [5].

Substantial evidence has shown that the heterogeneity of individual cells within a population is critical for cellular function and survival in the field of immunotherapy and cancer therapy [6]. Thus, high throughput single-cell analysis is of large interest to reveal cell-cell variability by elucidating molecular mechanisms at single-cell resolution. A number of single-cell analysis methods have been developed, such as optical tweezer, patch clamp, microscopic imaging, and flow cytometry [7–10]. In particular, flow cytometry has been beneficial to single-cell analysis by detecting and enriching cells that exhibit specific phenotypic markers [11, 12]. In addition, its high throughput in processing capability at a rate of thousands of cells per second makes it to be a great candidate for screening protein expression and surface markers through tagging with a fluorescent antibody or probe.

However, the need for fluorescent labeling of cells limits the breadth of capability to only endpoint analysis [13]. The features such as affinities, secretion dynamics, and cell-cell dynamic interactions are beyond the scope of flow cytometry.

The advent of microfluidic technology offers a set of tools that enables an integrated platform for a wide range of applications from single-cell compartmentalization, manipulation, and analysis [14–16]. Microfluidics is the science and technology of systems that involve channels with a dimension of tens of microns to manipulate fluids at an extremely small volume ranging from femto- to nano-liter. The length scale of microfluidic systems is comparable to the size of a single cell, which is around 10 μm in diameter and roughly 1 pL in volume. The capability to operate at such miniature dimensions in microfluidic systems is attractive and provides many unique advantages over existing single-cell analysis methods. The compartmentalization of single cells in small volumes can drastically improve the signal-to-noise ratio by reducing background noise, where it would be challenging to acquire the signal of individual cells from a bulk population [17, 18]. The capabilities in multiplexing and parallelization are also unique characteristics in microfluidic systems that made them suitable for single-cell analysis [19, 20].

Microfluidic technologies have been rapidly evolving for a growing number of single-cell applications, which can be further divided into three main categories based on how the single cells are compartmentalized: microvalves, micro/nano-wells, and droplets. These microfluidic platforms not only offer the capability to analyze individual cells, but also increase analysis efficiency, throughput, and reduce laborious tasks that are often associated with the traditional microtiter plate method. According to Web of Science as of 2021, the number of publications for single-cell analysis is rapidly and steadily increasing over the past

2

two decades for all three microfluidic platforms respectively (Figure 1 - 1). Particularly, droplet microfluidics has been an attractive method for single-cell analysis in a recent decade, as indicated by its number of publications that has surpassed microvalve- and microwell-based platforms.

Droplet-based microfluidic system provides an exceptionally powerful alternative for single-cell analysis, yet overcoming many limitations observed in bulk systems. Briefly, two streams of immiscible phases are introduced into a microfluidic device to generate monodispersed aqueous droplets that are stabilized by a continuous oil phase supplemented with surfactant. Instead of compartmentalizing single cells in microwells, droplet microfluidics exploits immiscible phases of aqueous reagent in an oil emulsion to generate pico- to nano-liter sized cell containing droplets. Since the advent of droplet microfluidic systems, it has gained substantial interest and development of tools for high-throughput bioassays owing to the unique abilities in generating monodispersed micro-droplets at a rate of thousands per second and eliminating cross-contamination [21]. This high rate of droplet generation provides flexible scalability to perform a large number of individual assays without being limited by any physical dimensional constraint or increasing complexity of a microfluidic chip, which leads to several orders of magnitude higher throughput as opposed to the aforementioned microfluidic systems. With the biocompatible aqueous and oil phase, the encapsulated cells can maintain their viability for an extended period of time in droplets. With the strengths of encapsulating cells in droplets as micro-reactors, droplet microfluidics provides more capabilities in isolating and analyzing single cells.
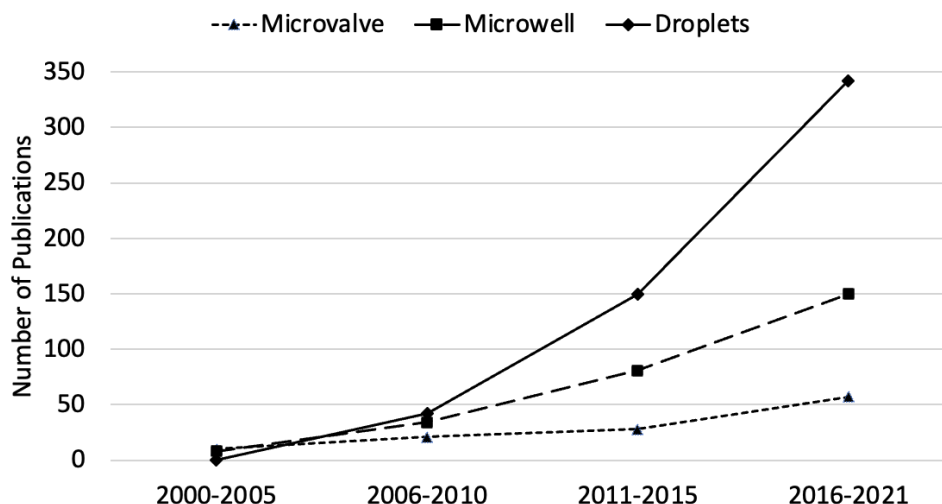
Figure 1 - 1 The number of publications from Web of Science from the year 2000 to 2021 on microvalve, microwell, and droplet microfluidics for single-cell analysis.

1.2 Fundamental of Droplet Generation

Droplet microfluidics is one of the sub-fields in microfluidics that generates and manipulates discrete droplets through two or more immiscible fluids through a microfluidic device. Many review literatures have been published that thoroughly describes the theoretical and various techniques of droplet generation, including active methods involving electrical, magnetic, thermal, and mechanical method [19, 22, 23]. This section will only highlight passive droplet generation that only relies on the channel geometry and hydrodynamic forces.

Droplet, as known as water-in-oil emulsion, is a mixture of two immiscible fluids, which is one of the important aspects in organic chemistry. Single emulsion is conventionally generated by vigorously agitating two immiscible phases in bulk. However, the distribution of shear force in bulk that is responsible for emulsification cannot be precisely controlled, resulting in highly polydispersity in size [24]. In contrast, microfluidics offers meticulously controlled of fluid flow to achieve monodispersed emulsions at the order of thousands per

second [21]. The encapsulation of target of interest in droplets that serve as microreactors can then be precisely manipulated, thus applicable for high-throughput biochemical and cellular analysis [25]. Thus, the capability of compartmentalization in a controlled manner makes droplet microfluidics to gain its important role in advancing single-cell analysis [21, 26].

Droplet generation is of essential step for various microfluidic applications. In passive method, two immiscible dispersed and continuous flows are driven by either syringe pumps that supply constant flow rates Q_d and Q_c or pressure pumps that provide stable constant pressure source P_d and P_c. When two immiscible phases meet at the droplet generation junction, the geometry of channel design defines the local flow fields, interface deformation, and droplet formation [19]. Depending on the channel geometry at the junction, droplet generation can be classified into co-flow, T-junction, and flow-focusing (Figure 1 - 2) [27]. Each geometry for droplet generation presents unique advantages, such as throughput and droplet size. Particularly, flow focusing provides broader range of control over droplet size with smaller size distribution compared to T-junction and co-flow methods. By adjusting the flow rates of two immiscible fluids, flow focusing has superior scalability with higher droplet generation rate, which is an important aspect for single-cell analysis. Thus, this dissertation will be focused on flow-focusing method.

At the droplet generation junction, the energy from the fluid driving force is partially converted into interfacial energy that introduces instability of the liquid-liquid interface, leading to shedding discrete droplets from dispersed phase [27]. The destabilization at the interface can be characterized by two competing effects, which are the extension and deformation of the interface induced by local shear stress (viscous force) and the resistance

of deformation from the interfacial tension. Thus, the interplay between viscous force and interfacial tension during droplet generation can be described by the capillary number Ca, as shown in Eqn. 1.1, where η is the dynamic viscosity, u is the characteristic velocity, and γ is the interfacial tension.

$$Ca = \frac{\eta u}{\gamma}, \qquad \text{(Eqn. 1.1)}$$

The capillary number Ca would be useful in predicting various regimes of droplet generation.

Generally, the droplet generation can be categorized into three regimes: squeezing, dripping, and jetting (Figure 1 - 3) [23]. Squeezing regime often occurs at low capillary number. The dispersed phase obstructs and protrudes through the droplet generating nozzle, thus transiently restricting the continuous flow around the developing protrusion. As the droplet is enlarging, the pressure gradient in continuous phase is also building up. Consequently, the growing pressure gradient in continuous phase becomes sufficiently large to overcome the pressure inside the forming droplet. The interface is then squeezed and cut by the continuous phase. As capillary number increases, the droplet generation regime would transition into dripping regime. In this regime, the viscous force is dominate over the interfacial tension and stabilizes the enlarging droplet against breakup. The droplet is generated at the flow focusing orifice due to Rayleigh-Plateau instability before the enlarging droplet obstructs the microchannel. Lastly, higher capillary number by increasing flow rate and viscosity of the continuous phase can result in jetting regime, which appears a long thread of dispersed phase fluid before breaking up into polydisperse droplets at downstream from the orifice.

Dr. Abraham Lee's lab has been one of the pioneers in droplet microfluidics by studying the phenomenon of droplet generation and the applications towards biological

applications. This dissertation will present different droplet microfluidic devices that overcome the limitation in co-encapsulation efficiency in droplets and advance the capability of droplet trapping for complex cellular analysis.
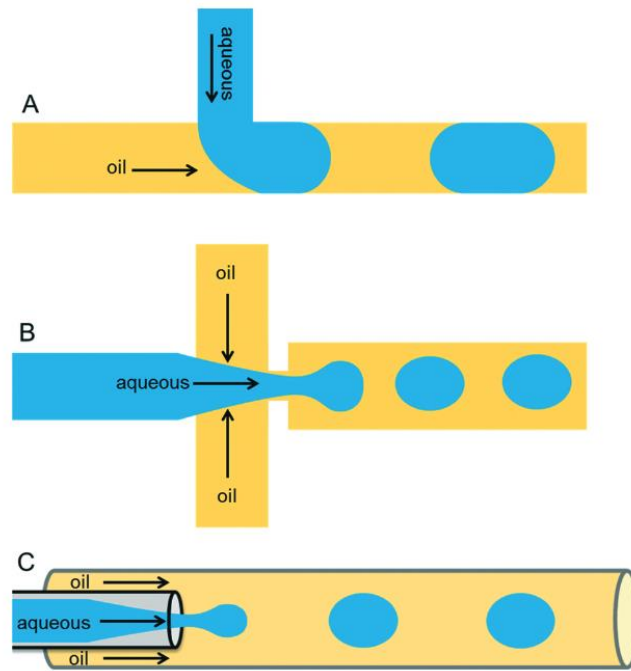
Figure 1 - 2 Different microfluidic droplet generation geometries. (A) T-junction geometry, as known as cross-flow, indicates that the flow of aqueous phase perpendicular to the flow of oil phase and sheared by the oil to generate droplets. (B) The flow-focusing geometry produces droplets by shearing the aqueous phase from two directions. (C) In the co-flow geometry, the aeuous phase is forced through a capillary, which is fabricated co-axially inside a bigger capillary [23].
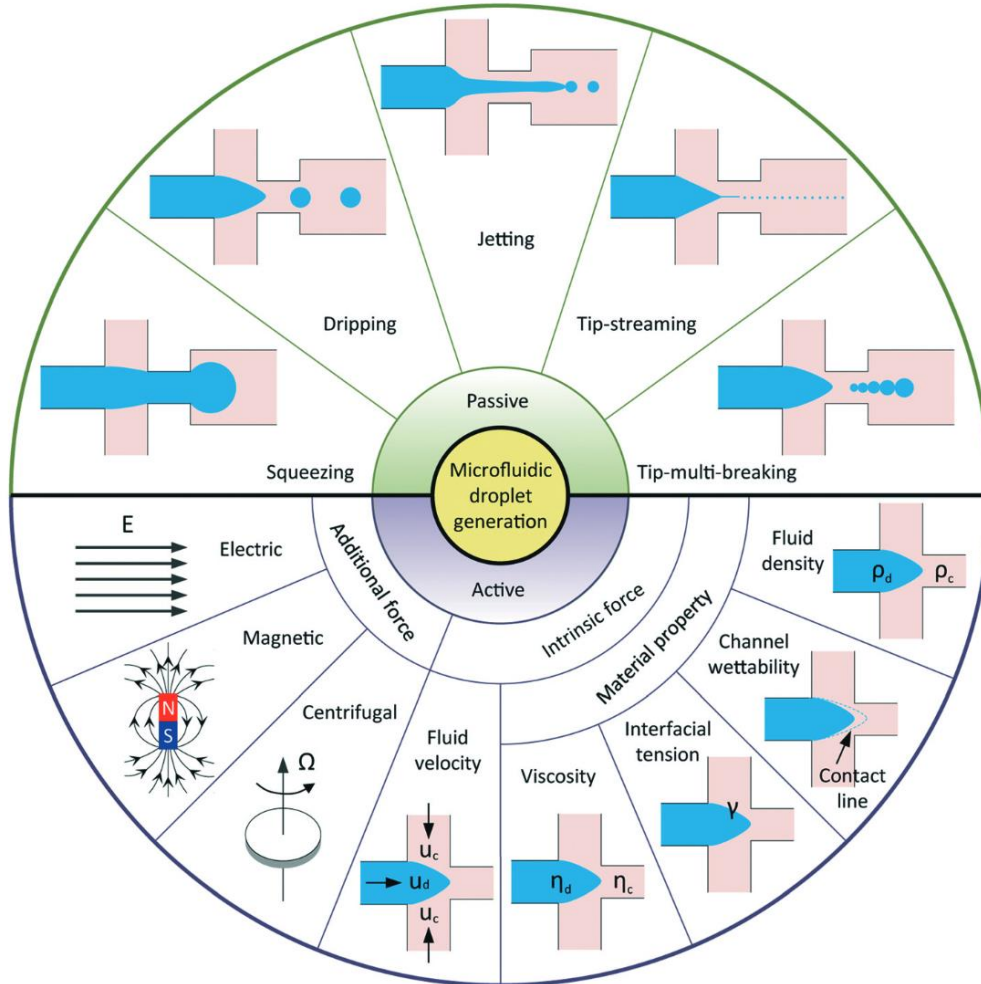
Figure 1 - 3 Schematic of droplet generation in passive and active methods. In passive method, droplet generation can be categorized into five regimes: squeezing, dripping, jetting, tip-streaming, and tip-multi-breaking regime. The type of droplet generation regime is dependent on the competition of capillary, viscous, and inertial forces [27]*.*

1.3   Overview of the Dissertation

This dissertation presents new droplet-based microfluidic platforms and strategies to address two aspects of the technical challenges for single-cell and cell pairing analysis: co-encapsulation efficiency and downstream cellular analysis in stationary droplet. The inefficient cell co-encapsulation and low platform versatility hinder the adoption rate of droplet microfluidics technology by biologists and industries. Thus, the development of passive, efficient 1-1-1 encapsulation platform without compromising simplicity, high-

throughput and versatility is greatly needed. The proposed microfluidic chip design takes advantages of hydrodynamics and close-packed ordering of cells to improve 1-1-1 encapsulation efficiency. The 1-1-1 encapsulation platform does not only significantly exceed double *Poisson* limitation but also accommodate samples with low cell densities. Furthermore, the advantages of 1-1-1 platform open a new avenue for large-scale analysis on cell-cell interaction. The improvement on efficient co-encapsulating cell pairs has direct implication in immunotherapy and a wide range of cell interaction assays.

In addition, this dissertation also presents a droplet trapping array device that contains a set of uniquely designed droplet traps for immobilizing cell-laden droplets. A continuous flow of oil is introduced to flow around the stationary droplets to induce microvortices inside the droplets by exerting shear force at the liquid-liquid interface. Thus, symmetrical microvortices in the aqueous droplets are observed that could facilitate the movement of the encapsulated particles or cells. To the best of our knowledge, this is the first report of a technique that utilizes continuous oil phase to modulate the encapsulated cells in droplets, and the internal flow dynamics of a stationary droplet that is subjected to continuous external oil flow is largely unexplored. Thus, the dynamics of induced microvortices and their associated parameters are explored in this research. The capability of controlling the cell movement within droplets provides a unique opportunity of studying immune analysis, where the transient scanning interaction and proximity between effector and target cell need to be deterministically regulated while retaining pairwise-correlated information to facilitate the study of immunological synapses. The trapped droplets enable long-term monitoring and temporal analysis of interaction between the encapsulated cell pair within an isolated microenvironment, which the conventional bulk method and

microfluidic cell traps cannot offer. Furthermore, the droplet microvortices also offer an alternative platform for the field of microscopy to reconstruct three-dimensional view of a cell instead of two-dimensional projection view by exploiting the rotating cell in droplet. As a result, these droplet-based microfluidic devices and strategies offer powerful tools for studying any biological applications involving single-cell and cell-cell interaction analysis, which are thereby directly applicable to a broad range of applications including immunotherapy, drug screening, and advance microscopy.

CHAPTER 2: Overcoming double *Poisson* limitation for co-encapsulation in droplets through hydrodynamic close packing of cells

2.1   Introduction

Single-cell analysis has emerged as an indispensable technique to reveal cellular heterogeneity within a cell population and enable profiling that bridges between phenotype and genotype [5, 28–31]. The field of single-cell analysis has gained tremendous interest from both academia and industry to further investigate the cell-cell variability for an accurate understanding of disease diagnosis and progression [32–34]. Beyond the interrogation of individual cells, the study of cell-cell communication offers in-depth information on deciphering dynamic and heterogeneous responses upon interacting with another cell [35–38]. As a plethora of evidence has shown the significance of heterogeneity within a clonal population, it is imperative to investigate the heterogeneity of cellular function and phenotype upon cell-cell interaction. In cancer biology, the cellular interaction between cancer stem cells and other cells within the tumor microenvironment has a major impact on cancer progression, survival, and lineage [36]. For instance, natural killer (NK) cell is a type of immune cells that can kill tumor cells, such as K562 cells, by inducing apoptosis upon interaction. The heterogeneous membrane marker expression of K562 can directly affects the cytotoxicity and proliferation of NK cells [39, 40]. This heterotypic cell-cell interaction within a confined microenvironment would facilitate the development of novel biomedical strategies such as immunotherapy or cell-based therapeutics for disease treatment [41–43].

The conventional method for studying cell-cell interactions involves bulk co-culturing in a flask either with or without cell-cell contact. Although the co-culturing system could achieve heterotypic or homotypic interactions by mixing different cell suspensions prior to

loading into a monolayer model, the number of interacting cells is difficult to be deterministically controlled [35]. Moreover, the mixed cells share the same environment, and cannot prevent cross-interference from the neighboring interacting cells. Bulk co-culturing also compromises sensitivity in detecting secretion from single cells due to high background noise and diffusion of secreted molecules into bulk medium. With these limitations, the analysis of single-cell upon cell-cell interaction becomes challenging.

In recent years, droplet microfluidics has been playing a catalytic role in the field of single-cell analysis spanning from genomic sequencing [44, 45], cytotoxicity screening [46], directed evolution of cell therapy [47], antibody discovery [48, 49], and monitoring of dynamic cell-cell interactions [50–52]. The compartmentalization of individual cells or cell pairs in monodispersed aqueous droplets that are suspended in an immiscible oil carrier fluid serves as micro-reactors and circumvents cross-interference from neighboring droplets. Droplets can be individually manipulated and interrogated for complex biological assays. Owing to the drastic reduction of volumetric confinement of cells in droplets, the secreted molecules from a single cell can quickly reach a detectable concentration, which improves the signal-to-noise ratio in comparison to the bulk co-culturing method [53, 54].

Although the workflow for encapsulating cells in droplets is relatively straightforward, single-cell encapsulation suffers an inherent fundamental challenge in its ability to control the number of cells per droplet. The randomly dispersed cell aqueous suspension is typically diluted prior to loading into droplets; thus, cell encapsulation statistics is often dictated by *Poisson* statistics (Figure 2 - 1a). Therefore, the distribution of the number of cells per droplet is governed by

$$P(k) = \lambda^k e^{-\lambda}/k!, \qquad \text{(Eqn. 2.1)}$$

where k is the number of cells in a droplet and λ is the average number of cells per droplet assuming complete random dispersion. Furthermore, the value of λ is directly proportional to the frequency of each cell entering the droplet generation junction and inversely dependent on the frequency of droplet generation rate (Eqn. 2.2).

$$\lambda = \frac{freq_{cell}}{freq_{droplet}}, \qquad (Eqn. \ 2.2)$$

The change in λ produces a different distribution of cell occupancy per droplet, where the number of droplets containing exactly one cell is maximized at 36.8% when λ is equal to one. Moreover, the fraction of droplets containing more than one cell becomes insignificant if the average number of cells per droplet is low ($\lambda < 0.3$). However, the fraction of empty droplets is then accounted for a significant majority of the droplet population that reduces throughput, wastes precious reagents, and complicates the subsequent analytical processes.

This stochastic encapsulation will lead to even more cumbersome and inefficient experiments in co-encapsulating one cell type A and one cell type B in one droplet, termed 1-1-1 encapsulation. Consider a random co-encapsulation of two distinct cells A and B with their respective cell density of λ_A and λ_B, the co-encapsulation efficiency is governed by double *Poisson* statistics (Eqn. 2.3).

$$P(k_A \cap k_B) = \frac{\lambda_A^{k_A} \exp(-\lambda_A)}{k_A!} * \frac{\lambda_B^{k_B} \exp(-\lambda_B)}{k_B!}, \qquad (Eqn. \ 2.3)$$

For 1-1-1 encapsulation efficiency, the *Poisson* limited single-cell encapsulation further reduces the probability of co-encapsulating two distinct cells per droplet to at most 13.5% under the optimal condition, whereas most droplets contain either no cells or incorrect cell pairing (Figure 2 - 1b). When compared with the common cell loading density that is typically used in FACS ($\lambda_A = \lambda_B = 0.3$), the 1-1-1 encapsulation efficiency can be only achieved as low

as 4.9%, and over half of the generated droplets (55%) contain no cells. Specifically, in cases where both cell densities are below one, the minimum of λ_A and λ_B dictates the maximum achievable 1-1-1 encapsulation efficiency and suggests a partially linear relationship (Figure 2 - 1c). Thus, the theoretical 1-1-1 encapsulation statistics with respect to the minimum of λ_A and λ_B illustrated in Figure 2 - 1d depicts a sigmoidal relationship for λ between zero and one.

To circumvent this *Poisson* limitation, both active and passive microfluidic techniques have been devised to improve the encapsulation process in the aspect of cell ordering or manipulation. Collectively, both existing techniques suffer either from high system complexity, low throughput, limited versatility, or poor encapsulation efficiency when encapsulating cells with low concentration. Active technique involves acoustic [55], optical [56], or magnetic force [57] to manipulate cells leading into the droplet generation region and actively generates droplets for cell encapsulation. The use of external force requires electrodes, actuators, or lasers to execute the operation, thus increasing the complexity of droplet generation process. These active methods also have a limited droplet generation rate that is orders of magnitude lower than passive encapsulation. In contrast, passive encapsulation merely relies on hydrodynamic effect and channel features, including inertial [58], viscoelastic effect [59], pinched flow fractionation [60], and gravitational field [61]. Specifically, passive techniques that rely on inertial or Dean force to achieve two ordered particle trains prior to co-encapsulation have been demonstrated with improved 1-1-1 encapsulation efficiency. However, the performance of these passive methods is critically dependent on the flow rates and the properties of particulates and fluids with the prerequisite of high cell loading density ($\lambda > 1$).

As the 1-1-1 encapsulation efficiency remains a significant technical challenge, we present a passive compartmentalization platform that leverages hydrodynamic draining for close packing of cells to overcome the limitation on double Poisson co-encapsulation efficiency. The presented draining technique in achieving close packing of cells offers simplicity and adaptability, which could increase platform compatibility for various reagents and lower cell loading density. In contrast to other passive methods, this platform is applicable to increase 1-1-1 encapsulation efficiency with the pairing of two different types of cells or with 1-cell and 1-bead encapsulated in a droplet.

d

Double Poisson Statistics of 1-1-1 Encapsulation
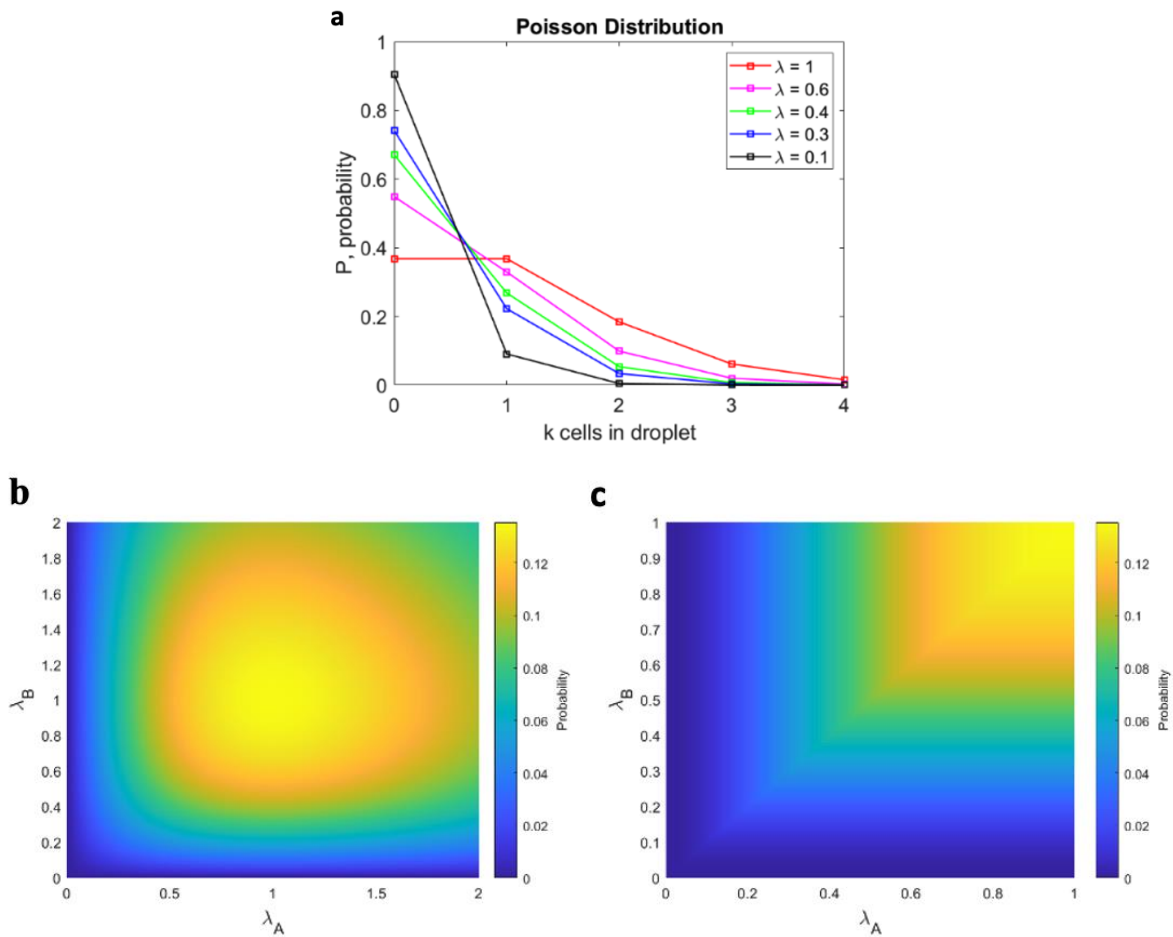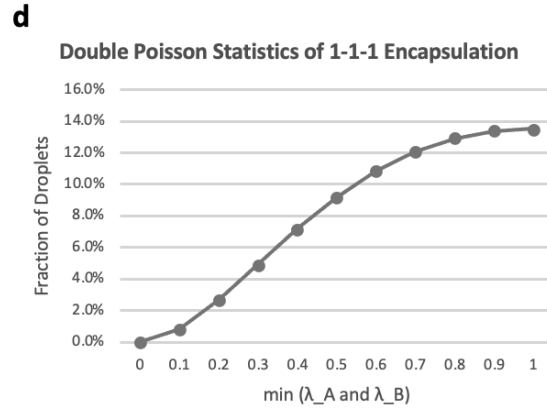
Figure 2 - 1 Poisson and double Poisson distribution. (a) Poisson distribution of single-cell encapsulation in droplets. (b)-(d) Distribution of double Poisson statistics for 1-1-1 encapsulation. (b) The probability to co-encapsulate two distinct cells in a droplet with respect to both λ_A average number of cells type A per droplet and λ_B cell type B per droplet. (c) The probability of 1-1-1 encapsulation efficiency with respect to both average number of cell A and B less than one (λ_A and $\lambda_B < 1$) and dictated by the minimum of λ_A and $\lambda_B < 1$. (d) The 1-1-1 encapsulation efficiency that follows double Poisson statistics exhibits a sigmoidal relationship against the minimum of λ_A and $\lambda_B = 1$.

2.2 Materials and Methods

2.2.1 Microfluidic Device Design

The 1-1-1 co-encapsulation microfluidic device consists of four inlets and two outlets as illustrated in Figure 2 - 2. Three of the four inlets are used for the perfusion of aqueous phases, including two for separate cell loading and one for sheath flow, whereas the remaining inlet is for the perfusion of continuous oil phase. The two outlets serve as droplet collection and aqueous draining for the cell loading streams, respectively. Both the aqueous and oil phases are delivered into the microfluidic device at a constant volumetric flow rate, where the draining outlet withdraws the aqueous phase at a constant volumetric flow rate.

The flow of each cell suspension solution, Q_{cell}, enters the device and passes through a narrow channel with a width of 20 μm and a height of 40 μm. These channel dimensions facilitate the self-assembly of a randomly dispersed cell suspension into a centered single-

16

cell train. Each cell train subsequently moves toward the drainage junction for close packing. As two cells with initial distance L within a cell train subsequently enters the junction, the flow stream Q_{cell} splits into three directions that flows toward both sides of the draining channels Q_{drain} and downstream for encapsulation $Q_{cell,drain}$. The volumetric flow rates before and after are equal due to the conservation of mass, which can be described as

$$Q_{cell} = 2 \times Q_{drain} + Q_{cell,drain}, \qquad \textit{(Eqn. 2.4)}$$

Given the volumetric flow rate is the product of channel cross-sectional area A and velocity v or $Q = Av$, the Eqn. 2.4 can be described as

$$(v_{cell} - v_{cell,drain})A_{cell} = 2 \times v_{drain}A_{drain}, \qquad \textit{(Eqn. 2.5)}$$

where the cell stream channel cross-sectional area A_{cell} is the same for before and after drainage junction. With absence of draining, the velocity of a cell is the same for before and after drainage, where $v_{cell} = v_{cell,drain}$. When $v_{drain} > 0$, the velocity of a cell decreases after the drainage junction due to $v_{cell} - v_{cell,drain} > 0$. While a fraction of Q_{cell} is diverted into two draining channels, the velocity of the leading cell decreases as the trailing cell catches up. At a given drain rate, this transient discrepancy of velocity between the leading and trailing cell results in the initial cell-cell distance L shortening by a distance of δ until the trailing cell also enters the drainage junction, which leads to close packing of cells with a cell-cell spacing of $L - \delta$ as the cells exit the drainage region. The shorten distance δ increases as the drain rate increases that further reduces the cell-cell spacing. The shortened cell-cell spacing effect from drainage junction improves the cell loading process by attaining higher on-chip cell density prior to entering the droplet generation junction, which plays a vital role in enhancing 1-1-1 encapsulation efficiency.

Each drainage junction contains a pair of pillar arrays with 10 μm gap that are positioned on both sides of the channel at a 45º backward angle with respect to the flowing direction. The bilateral draining flows withdraw a fraction of the solution of cell suspension while retaining cells inside the channel. All draining flows are designed to maintain equal hydrostatic pressures and flow rates, where the bifurcation channel design with equidistance from the draining outlet to the four draining channels is employed to ensure equivalent channel resistance. The balanced pressure on both sides of the draining junction is imperative to mitigate cells from escaping the channel to prevent adverse cell loss. In addition, the backward drainage angle of the pillar array acts as a filter and induces microvortices to pivot any escaped cells back into the channel. The process of draining a fraction of Q_{cell} does not only increasing on-chip cell density but also effectively reduces the longitudinal spacing between cells. Due to the increased cell density and shortened cell-cell spacing, the λ value of its respective cell type also increases which results in improving the probability of 1-1-1 encapsulation and attenuating the number of empty droplets.

Both cell trains with shortened cell spacing merge with the sheath flow, where it focuses both cell trains to its respective side of the channel. Given the nature of laminar flow at a low Reynolds number in microfluidic devices, the sheath flow acts as a divider to separate two cell trains to prevent premature interaction before co-encapsulation. In addition, bioassay reagent of interest could also be used as the sheath flow to warrant a temporal control of a reaction. The sheath flow and two streams of cell trains collectively interface with the continuous oil phase at the nozzle to form droplets. The immiscible oil phase symmetrically exerts interfacial shear at the aqueous stream to form droplets at a rate

that is optimized for the rate of the cell arriving frequency. The flow rate control of Q_{Cell} and

the regime of droplet generation are discussed in the Results and Discussion section.
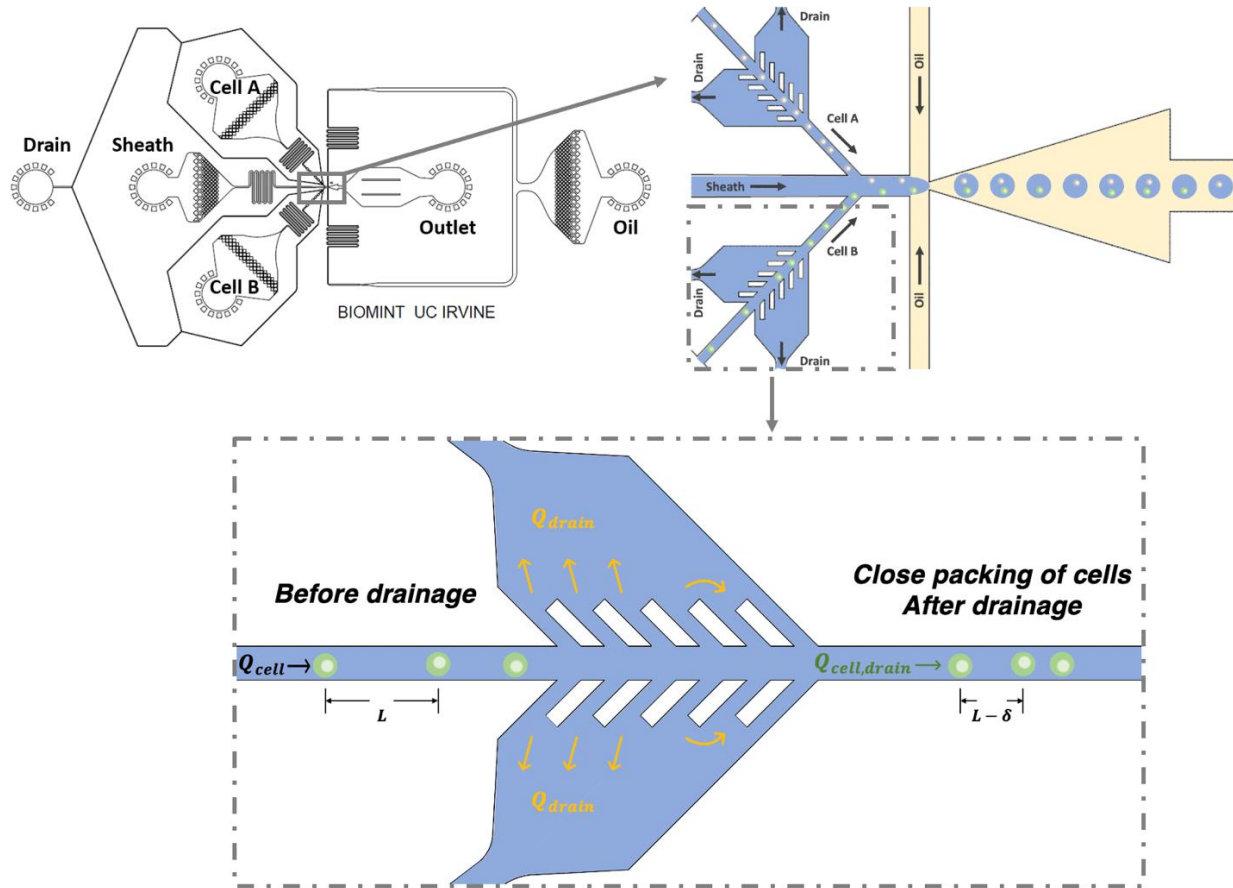
Figure 2 - 2. Design principle of passive 1-1-1 encapsulation device. (a) Schematic of the passive 1-1-1 encapsulation device that consists of four inlets (two cell suspensions, one sheath flow, and one oil) and two outlets (drainage and collection). (b) Close-up schematic of the 1-1-1 encapsulation device of the drainage and droplet generation junction. The single-filed close packed cell trains merge with sheath flow at the main channel and collectively enter the high shear droplet generation junction to form aqueous droplets upon contacting the immiscible carrier oil. (c) An initial distance L between the leading and trailing cell enters the drainage junction. The effect of draining causes close packing of cells that results in the initial cell-cell distance L shortening by a distance of δ until the trailing cell also enters the drainage region.

The microfluidic devices were fabricated in polydimethylsiloxane (PDMS, Sylgard 184, Dow Corning) following standard soft lithography. The channel geometry was designed in computer-aided design software (AutoCAD) and printed on mylar masks through CAD/Art Services as illustrated in Figure 2 - 3. The 4-inch silicon wafer substrates were spin-coated with SU-8 2050 negative photoresist (MicroChem) to achieve the height of 40 μm and subsequently patterned by ultraviolet exposure for crosslinking to form a master mold. The photolithography process follows the recommended MicroChem protocol. Prior to soft lithography, the mold with channel patterns is spin-coated with a mixture of PTFE (polytetrafluoroethylene) and FC40 (a ratio of 1:5) at 3000 rpm for 30 seconds. Subsequently, the mold is incubated in oven at 120 degrees Celsius for 1 minute to ensure thorough evaporation. The coating of this mixture can prevent the adhesion of PDMS to the wafer during the lift-off process during soft lithography. Polydimethylsiloxane (PDMS) elastomer was mixed with curing agent at a 10:1 ratio and degassed before pouring onto the master mold, followed by curing at 65 $^\circ$C overnight for complete crosslinking. The PDMS molded imprints and glass microscope slides were oxygen plasma treated (Harrick Plasma Inc) for 2 minutes and bonded together to form a permanent seal. The devices were baked in an oven at 120 $^\circ$C overnight to secure their natural hydrophobicity.

a

Cell *A* Inlet

Draining Outlet

Sheath Inlet

Collection Outlet

Oil Inlet

V10 D4

BIOMINT UC IRVINE

XLUO CELL PAIRING v10

Cell *B* Inlet

b

Cell Type B

Aqueous Sheath Flow

Cell Type A

0.0100

0.0198

0.0400

0.0200

Oil Phase

Oil Phase

0.0150

0.1000
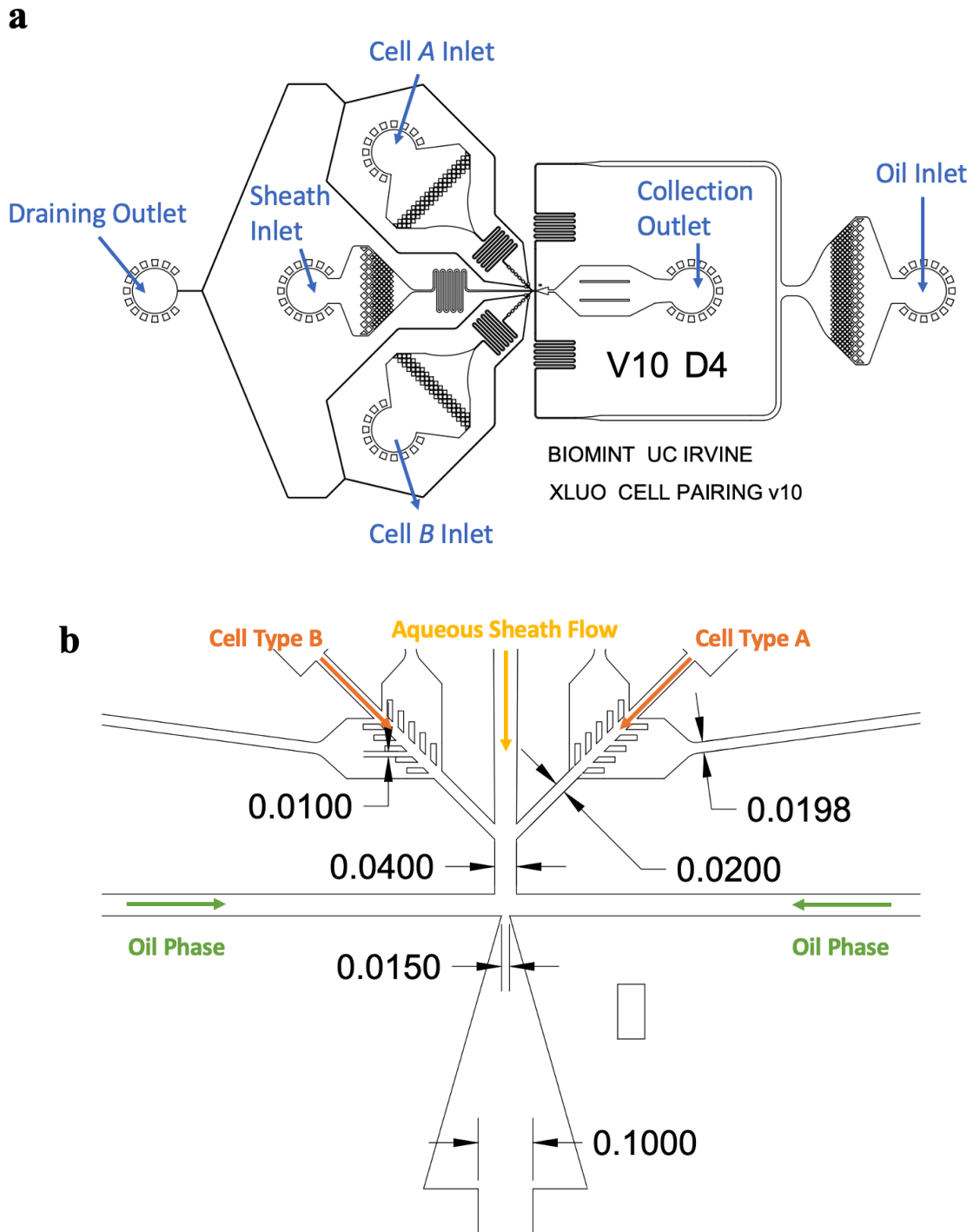
Figure 2 - 3 Channel design: AutoCAD drawing and channel dimension specifications. (a) AutoCAD schematic of the 1-1-1 co-encapsulation device illustrates the three aqueous phase inlets (sheath, cell type A, and cell type B), one inlet for oil phase flow, one draining outlet, and one collection outlet. (b) The enlarged image of (a) at the droplet generation junction with channel width dimensions. The labeled dimensions are measured in the unit of millimeter.

2.2.3 Cell Culture

Human erythromyeloblastoid leukemia cells K562 (American Type Culture Collection (ATCC)) were used to assess the performance of 1-1-1 encapsulation. K562 cells were cultured in a T-75 cell culture flask using RPMI 1640 medium (Gibco) supplemented with 10% (v/v) fetal bovine serum (Gibco), and 100 U/mL penicillin-streptomycin (Gibco). The cells were cultured in a condition of 5% CO_2 humidified incubator at 37 ºC and passaged every 2-3 days with a seeding density of 1×10^6 cells/mL. In preparation for encapsulation, the aqueous phase solution was prepared in RPMI medium supplemented with 16% Optiprep, 1% BSA, 0.01% Triton X-100, and 10 U/mL of DNase I, which would serve as sheath flow and cell suspension. The addition of Optiprep density gradient medium is essential to prolong the sedimentation time of cells in aqueous suspension. The BSA and DNase I in the aqueous phase can also mitigate the aggregation of any unspecific binding of cells and digest the DNA that was released from the dead cells, which can avoid the potential of channel clogging issue due to cell aggregates. Subsequently, the cells were resuspended in the aqueous phase mixture at a desired volume fraction, ranging from 2 to 2.5%. For the continuous phase, 2% (w/v) 008-FluoroSurfactant in HFE 7500 oil (Ran Biotechnologies) was used.

2.2.4 Experimental Setup

Cell suspensions, sheath flow solution, and oil were separately loaded into the microfluidic co-encapsulation device using four 1 mL plastic syringes (BD, Breda, Netherlands) and were connected to their respective inlets with PTFE tubing (Cole Parmer, ID 0.022 inch and OD 0.042 inch). A syringe filled with aqueous solution was connected to the drainage outlet with PTFE tubing, in which the absence of air in a syringe would prevent

any gas contraction or expansion to ensure a constant drain rate. Lastly, PTFE tubing was connected to the outlet of the device to direct droplets into a collection Eppendorf tube. Both the dispersed phase and the continuous phase are delivered into the microfluidic device at constant volumetric flow rate and individually controlled by syringe pump (Pico Plus; Harvard Apparatus, Inc., MA, USA). Syringe pump as flow control system is desirable due to its consistent volumetric flow delivery and independent of channel resistance. The flow rate of the continuous oil phase was set at 5 µL/min, and the dispersed aqueous phase for cell was set at 3-3.5 µL/min. The sheath flow was initially set at 1 µL/min and could be adjusted to tune the droplet generation rate as needed. The syringe for draining was mounted on a syringe pump with withdrawal mode at a flow rate of 0-2.5 µL/min to remove the aqueous solution.

The microfluidic chip was mounted onto the stage of a Nikon 100-S inverted microscope and monitored using a computer-controlled high-speed Phantom camera V-310 (Vision Research, Wayne, NJ) for image recording. Droplet generation videos were acquired at 10,000 frames per second to ensure aliasing due to down sampling. A customized MATLAB code was utilized to assess cell-cell longitudinal spacing. To obtain co-encapsulation statistics, we analyzed the high-speed videos frame by frame during cell co-encapsulation by using ImageJ, a public domain Java-based image processing software program developed at the National Institutes of Health.

2.3   Results and Discussion

2.3.1   Droplet Generation Rate for an Effective 1-1-1 Encapsulation

The droplet generation rate is a function of flow rates of both dispersed and continuous phase, size dimensions of a nozzle, and interfacial tension. Droplet production processes have a direct impact on the efficiency of 1-1-1 encapsulation of cells, which is critical to understand the rate of droplet generation with respect to its associated parameters. A large discrepancy between droplet generation frequency and cell arrival rate at the nozzle can be detrimental to the overall encapsulation efficiency. Thus, the effect of droplet generation frequency and cell arrival rate are investigated for various flow rates for optimal 1-1-1 encapsulation.

The droplet generation frequency exhibits a positive relationship as the flow rate of dispersed phase increases, as well as the increasing of continuous oil flow rate (Figure 2 - 4a). The results are congruent with the physics theory of droplet generation, where the modes of droplet formation can be determined according to the capillary number *Ca*.

$$Ca = \frac{\mu U}{\gamma}, \qquad (Eqn.\ 2.6)$$

The capillary number *Ca* is a non-dimensional quantity and is dependent on viscosity μ and characteristics velocity U of the continuous phase and surface tension γ of the water-oil interface. With the increasing value of *Ca*, the mode of droplet generation would be in transition in the order of squeezing, dripping, and jetting regime.

In the dripping regime, the *Ca* number is high enough, such that the droplet formation is shear dominant with a generation frequency in the order of thousands of droplets per second. Particularly, the droplet generation frequency reaches roughly 7,000 droplets per second on the 1-1-1 encapsulation device (Figure 2 - 5a). This high droplet generation

frequency would lead to an exceedingly low λ value according to Eqn. 2.2, which results in generating a plenitude of empty droplets. Such a high fraction of empty droplets is challenging to be offset by the number of droplets containing correct pairing, which conversely undermines the efficiency of 1-1-1 co-encapsulation. Despite higher cell loading density or flow rate Q_{cell} could increase the frequency of cells arriving at the nozzle, this method can often lead to channel clogging from highly concentrated cell suspension or excessive shear stress at high flow rate. In the squeezing regime when the Ca value is low, the tip of dispersed phase transiently blocks the nozzle and protrudes outward into the continuous phase. The neck of the interface is squeezed from the increased pressure until it breaks off (Figure 2 - 5b). This mode of droplet generation offers a relatively slower generation frequency near or below one thousand droplets per second that is suitable for encapsulating cells with lower cell loading density.

For a passive device, the droplet generation rate could not be actively modulated to accommodate any fluctuation of cell arrival rate due to intrinsic random dispersion of cells. However, the droplet generation in squeezing regime can tolerate for the fluctuation of cell spacing without adversely compromising droplet throughput. Assuming cells are uniformly dispersed, the analytical simulation on the arrival rate of cells at droplet generating nozzle demonstrates a positive linear relationship with the flow Q_{cell} for various cell density (Figure 2 - 4b). Consider the cell loading density of 10×10^6 cells/mL with local cell density fluctuation between 5 to 15×10^6 cells/mL, a Q_{cell} flow rate of 8 µL/min can trigger an extensive range of cell arrival frequency in comparison to the one with slower flow rate. Due to the fixed droplet generation rate, this broad range of cell arrival frequency would lead to large number of droplets with incorrect encapsulation. Slower flow rate Q_{cell} is optimal as it

presents a narrower range of cell arrival frequency. Furthermore, the cell arrival frequency for high flow rate Q_{cell} can quickly reach over one thousand cells per second that demands a higher droplet generation rate in dripping regime. The droplet generation rate over a thousand droplets per second can lead to a plethora of empty droplets. Thus, a slower flow rate Q_{cell} does not only lead to a narrower range of cell arrival rate despite the fluctuation of cell density but also falls in the same order of magnitude with the rate of droplet generation in squeezing regime. Lastly, the modulation of flow rate in sheath flow enables a fine adjustment of droplet generation rate. As a result, the droplet generation in squeezing regime and slower flow rate Q_{cell} are chosen for the assessment of the 1-1-1 encapsulation platform.

a
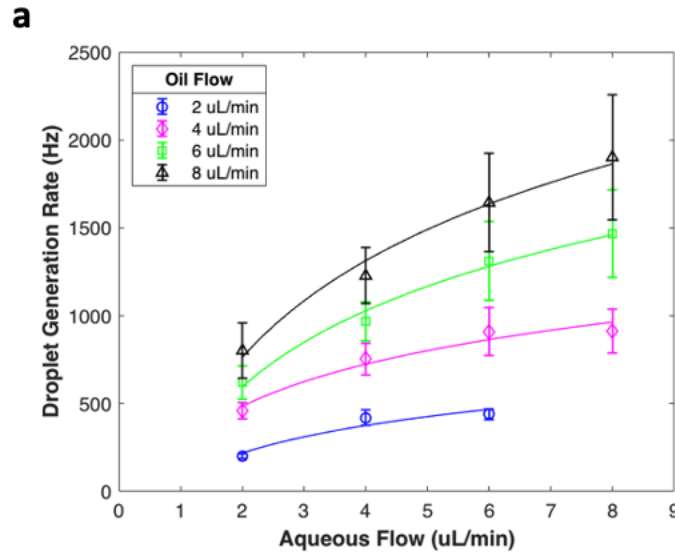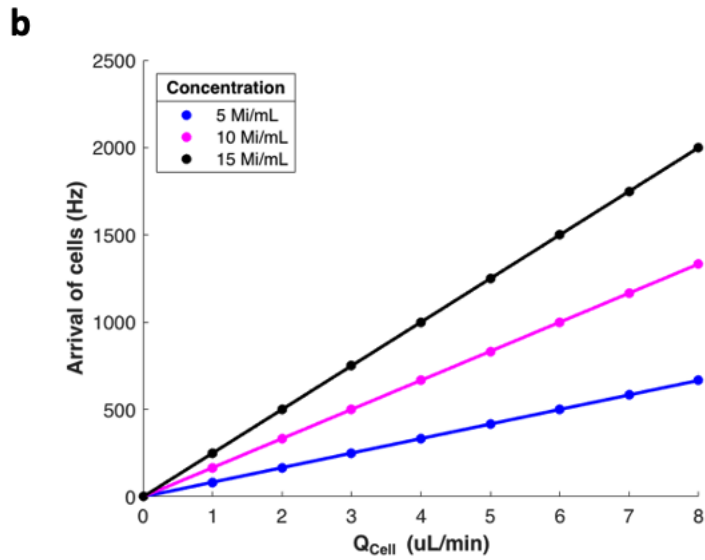
Figure 2 - 4 Droplet generation characterization analysis (a) Characterization of droplet generation frequency with respect to various aqueous and oil flow rate. (b) The arrival frequency of cells at the droplet generation nozzle is approximated under the assumption of uniformly dispersed cells. The frequency difference among various cell concentrations increases as the cell flow rate increases.
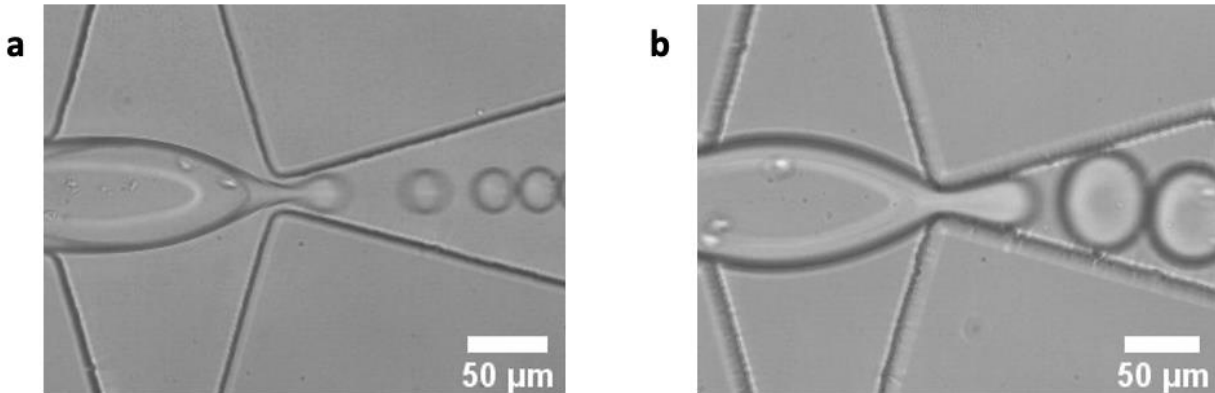
Figure 2 - 5 Comparison of droplet generation under dripping and squeezing regime (a) Droplet generation at squeezing regime, where the liquid-liquid interface makes contact at both sides of the nozzle before breakoff. (b) Droplet generation at dripping regime, where the droplet formation is shear-dominated by the continuous phase and the liquid-liquid interface separates from the nozzle.

2.3.2   Self-assembly of Cell Trains through Close Packing

The drainage junction consists of pillar arrays on both sides of each cell channel, which enables balanced drain rates and pressures that are exerted on each passing cell to mitigate the occurrence of cells escaping the channel. The pillar array serves as a filter with

10 μm gaps and is slanted at a 45° angle backward with respect to the flow direction. We discovered that this pillar design could induce microvortices to redirect any escaped cells back into the cell channel to further prevent cell loss. A computational fluid dynamic simulation was performed to analyze the velocity flow fields at the drainage junction. Single phase creeping flow module was utilized for the simulation, where the flow rate Q_{cell} was set at 2 μL/min and the total drain rate at 1.25 μL/min. At the drainage junction, the flow Q_{cell} is divided into three different directions, such that the cell suspension solution either flows straight to merge with the sheath flow downstream or diverts to the pillar arrays on both sides. The velocity field indicates that the angle of pillar position facilitates the formation of recirculation at the downstream part of the array (Figure 2 - 6). In addition to the equal drain rates, the recirculation is beneficial to further mitigate cell loss to redirect the escaped cells back into the flowing stream. The drain rates tested in the experiments did not present any significant cell loss from the cell suspension solution. However, exceedingly high drain rate could contribute a detrimental effect on cell loss, where majority of the cell suspension solution would preferentially flow toward the pillar arrays on both sides. This is attributed to the lower channel resistance of the pillar arrays in comparison to that of the cell channel, where the cross-sectional area of the pillar arrays is six-fold of the cell channel. Thus, the optimization of the draining rate and the flow Q_{cell} is imperative for achieving an effective close packing of cells.

To evaluate the efficacy of close packing of cells from the drainage junction, a custom-made MATLAB script was developed to analyze the distance of cell spacing. Briefly, slow-motion videos captured by the high-speed Phantom camera were used to analyze each frame. The grayscale frames were converted into binary format, which enables the identification of

cells. Subsequently, two regions of interest were selected at the channel entrance and exit of the drainage junction to detect the arrival of cells. When a cell crosses the region-of-interest area, a spike of pixel color will be detected. Peak-to-peak analysis was utilized to obtain the statistics of spacing between cells.

For cell spacing analysis, a suspension of K562 cells was delivered into the device at a constant flow rate of 3 µL/min, and three different draining flow rates (0, 1.25, and 2.5µL/min) were examined. No significant difference was observed in cell spacing before and after the drainage junction in the absence of draining (Figure 2 - 7a). Each passing cell flows at the same velocity across the drainage junction as no volume of cell suspension is removed, thus the lack of velocity difference between cells results in δ to be zero. Conversely, the presence of drain rate removes a fraction of cell suspension volume that leads to differential in the velocity of flowing cell before and after the drainage. This velocity difference between the leading and trailing cells within a cell train leads to the positive value of δ that shortens the cell-cell distance. In addition to both drain rates of 1.25 and 2.5 µL/min showed a substantially shortened cell spacing after drainage junction (Figure 2 - 7b and 7c), the value of δ is also dependent on the level of drain rate. As high volume is being removed in the drain rate of 2.5 µL/min, the velocity of a leading cell would be lower in comparison to that of a drain rate of 1.25 µL/min, which increases the time for a trailing cell to catch up and increases the value of δ for shortening cell-cell spacing. Consequently, the drain rate of 2.5 µL/min indicates nearly half of cell-cell spacing reduction across a drainage junction, where there is 21% reduction for drain rate of 1.25 µL/min. According to Figure 2 - 7d, an average cell-cell spacing before drainage junction is around 200 µm, which is equivalent of a cell arrival rate of 300 cells per second. The drain rate of 2.5 µL/min effectively enhances the

on-chip cell density that results in a 21% increase of cell arrival rate. Thus, the drainage junction can effectively close pack a randomly dispersed cell train to a level that minimizes the number of empty droplets when the droplet generation rate is fixed.

Although the drainage junction reduces the cell-cell distance of δ, the intrinsic random cell spacing persists with decreased range of dispersion. With a more regulated cell-cell spacing, the frequency of droplet generation is crucial to accommodate the random dispersed cell train. As the cell arrival rate after drainage junction is roughly 400 cells per second, the droplet generation rate is set at a rate of a thousand droplets per second. At this droplet generation rate, it can accommodate the randomness of cell-cell spacing that minimizes the fraction of droplets with more than 2 cells of the same cell type. Therefore, the increase of cell arrival rate and narrower range of cell-cell spacing contribute to the improvement of 1-1-1 co-encapsulation efficiency.
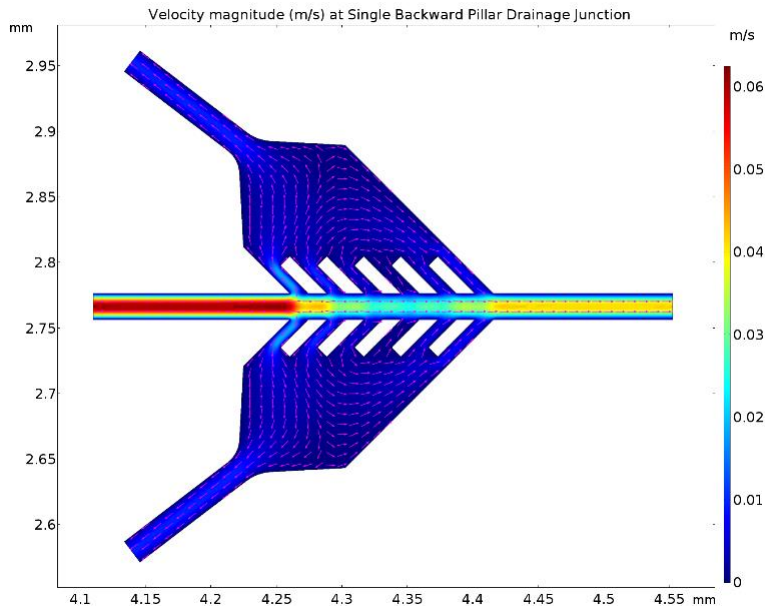
Figure 2 - 6 Numerical simulation of drainage junction showing velocity flow field under the effect of draining. Two recirculation vortices were induced with the pillars positioned 45 degrees backward with respect to cell flow direction, which can serve to re-direct escaped cells back into cell channel.
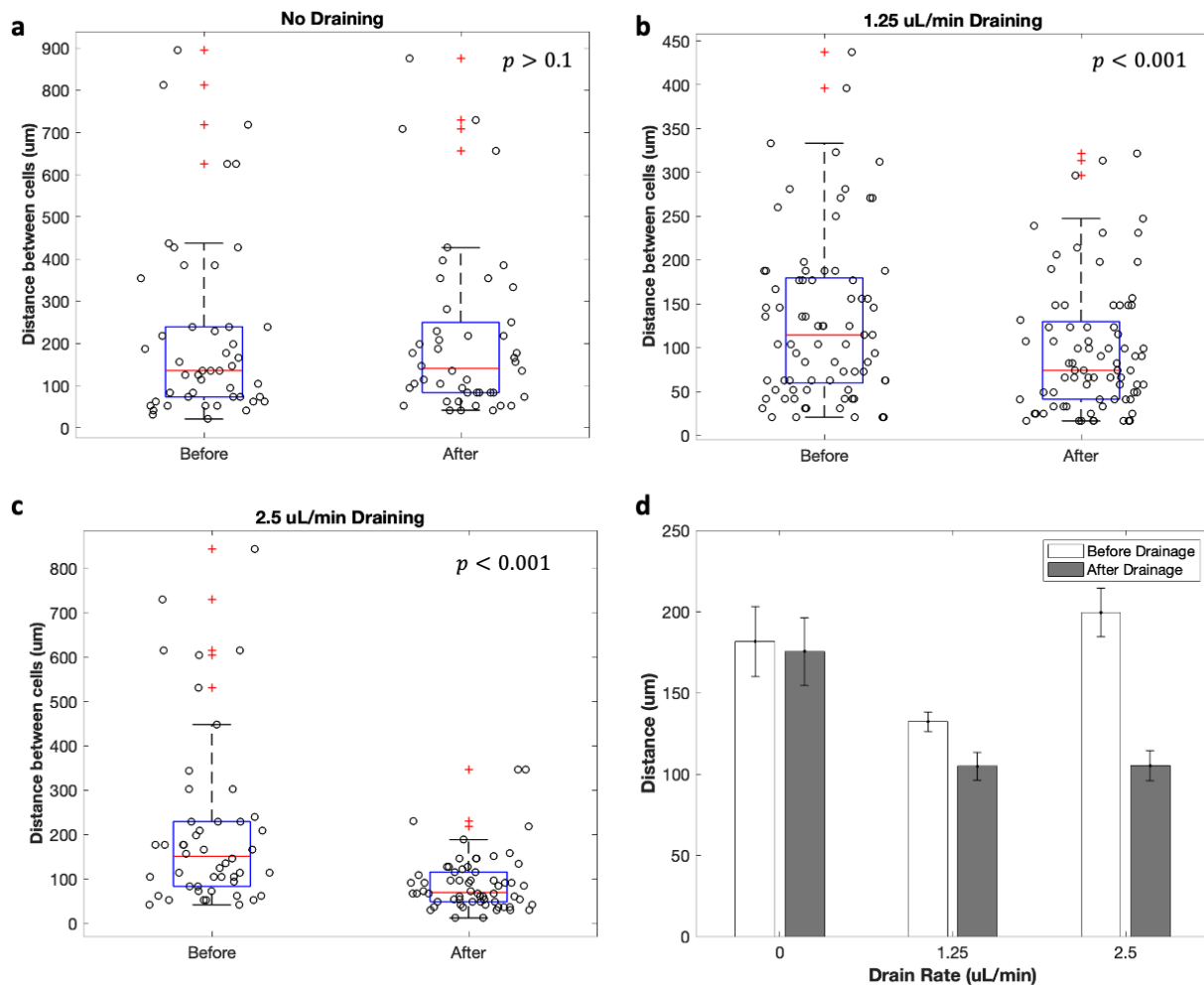
Figure 2 - 7 Cell spacing assessment on drainage effect using 3μL/min cell flow rate of K562 cells in 10 million/mL density and various drain rates. (a) With no draining, the cell spacing does not show any statistical difference in before and after drainage junction (p>0.1). (b) The drain rate of 1.25μL/min demonstrated a significant shift in cell spacing after the drainage junction (p<0.001). (c) The cell spacing distance was significantly shortened under the drain rate of 2.5μL/min (p<0.001). (d) The average cell-cell spacing under various drain rates 0, 1.25, and 2.5μL/min (N=3).

2.3.3   Assessment of 1-1-1 Efficiency

The 1-1-1 encapsulation device was applied to co-compartmentalize K562 cells with two different densities to demonstrate performance (Figure 2 - 8a). Each flow rate of cell suspension solution was set to 3 μL/min with a draining rate of 2.5 μL/min, whereas the

sheath flow and continuous oil were respectively flowing at 1 µL/min and 5 µL/min. See the high-speed video recording of the co-encapsulation in the supporting information. The droplet generation frequency was maintained at around 980 droplets per second, which resulted in the expected number of cells per droplet to have a λ value of 0.4 for the given cell loading densities. The encapsulation probability for both cell channels is illustrated in Figure 2 - 8b in comparison with its theoretical single-cell *Poisson* distribution. The increase in cell arrival rate led to the improvement of single-cell encapsulation efficiency to be as much as 43% with respect to *Poisson* statistics. The close packing of cells decreases the overall cell-cell spacing, which reduces 23% on the number of empty droplets for both channels. The enhancement of single-cell encapsulation and reduction on the number of empty droplets directly relate to the improvement on the 1-1-1 encapsulation efficiency.

Owing to the benefits of drainage junction, the 1-1-1 encapsulation efficiency achieved as high as 21% of the droplets contain correct pairing, whereas the double *Poisson* efficiency is only 12%. The overall co-encapsulation statistics over three separate experiments with cell density of $\lambda \approx 0.4$ is normalized against the double *Poisson* (Figure 2 - 8c). The 1-1-1 encapsulation devices were performed to yield an average of over 2.3-fold improvement in 1-1-1 encapsulation efficiency, which exceeds the intrinsic limited double *Poisson* statistics. One strong assumption behind the *Poisson* distribution is that cells arrive independently in droplets. This is not the case as soon as there are interactions between cells, for instance, cells adhere to each other that are closely packed as they are delivered into the microfluidic device. Such an increase in 1-1-1 encapsulation efficiency is the result of the packing of cells upon entering the droplet generation junction, which also resulted in the increase of λ values of cell loading density. In addition, the distribution of the number of cells

per droplet demonstrates that over 38% reduction in the number of empty droplets, which is consistent with the single-cell encapsulation results in Figure 2 - 8b. The fraction of single-cell cell during co-encapsulation is comparable with the double *Poisson* statistics, whereas an increment in the fraction of droplets containing three or more cells per droplet was observed. Despite the increase on the number of droplets with multiple cells, it only constitutes only 8% of the total droplets. This observation is the result of close packing of cells prior to encapsulation. As a result, the technique of hydrodynamic draining to achieve close packing of cell can overcome the double *Poisson* limitation with over 2.3-fold improvement in 1-1-1 encapsulation efficiency, which indicates the robustness of the performance.
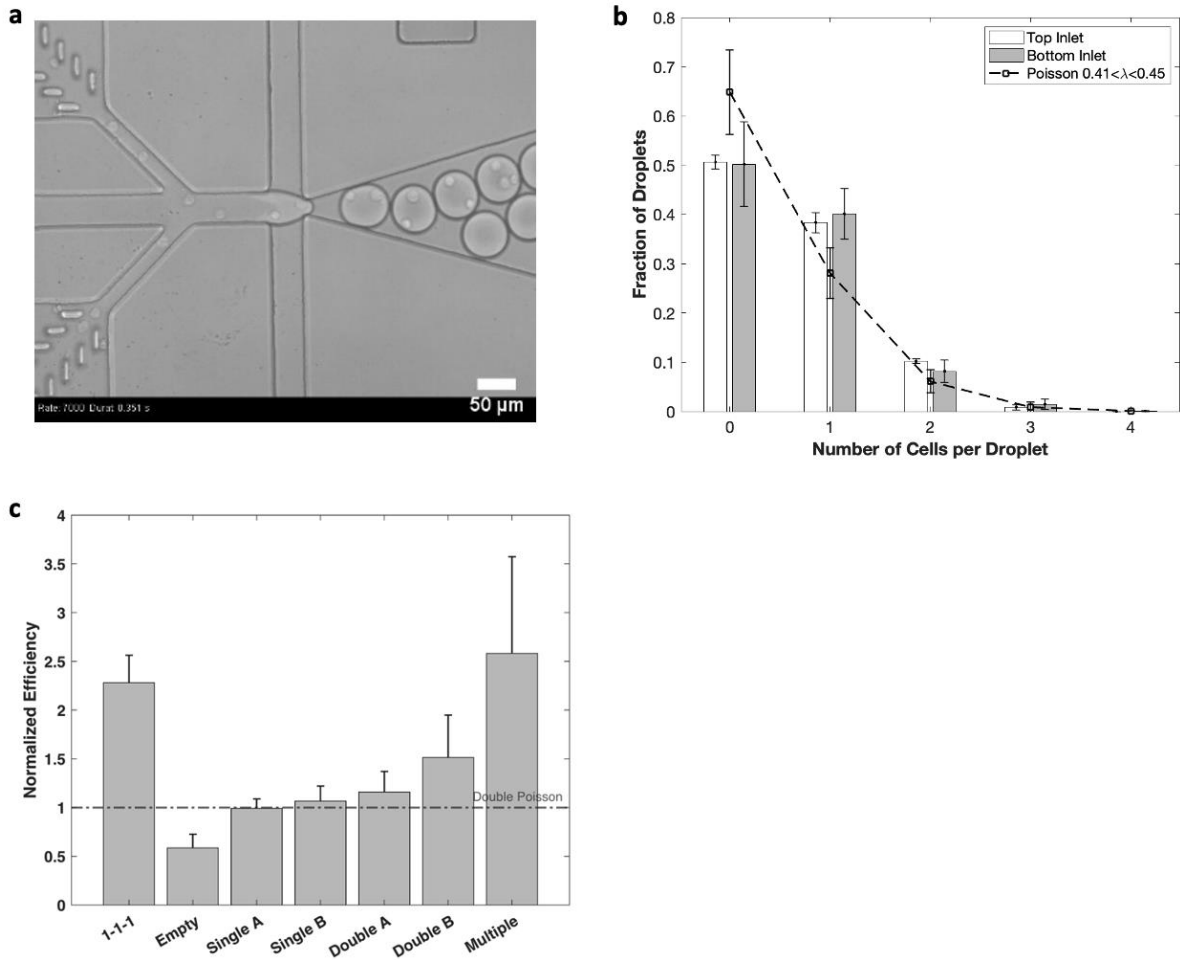
Figure 2 - 8 Encapsulation statistical analysis on 1-1-1 encapsulation device. (a) Bright-field microscopic image demonstrates the co-encapsulation of cells in monodispersed droplets. (b) Comparison of the distribution on various number of cells per droplet against Poisson statistics with $\lambda = 0.4$ (N=3 with average 210 droplets). (c) Distribution of experimental co-encapsulation statistics normalized against double Poisson distribution (N=3 with average 210 droplets).

2.4   Conclusion

In this work, we presented a passive microfluidic device that utilizes close packing of cells through draining of aqueous phase and hydrodynamic sheath flow for single-file cell trains prior to droplet generation. With these passive techniques to achieve the ordering of cell trains, the cell-cell distance has been substantially shortened to reduce the fraction of empty droplets. Another notable feature of this technique is that it could perform high-

efficiency co-encapsulation at low cell concentrations ($\lambda < 1$), and this platform is all passive, controlled only by the flow rates of the two phases, which does not require complex channel structures or active elements. Thus, the resulting 1-1-1 co-encapsulation efficiency surpasses the double *Poisson* limitation by over two-fold improvement for pairing two separate cells in droplets at 1 kHz rate. Furthermore, the improved encapsulation efficiency in single cell and cell pairing from this platform would be particularly beneficial for cell-cell pairing analysis by providing an abundance of useable droplets for various control groups during cellular analysis. One limitation of this technique is the intrinsic random dispersion of cells where the fluctuation of cell density is too large. Extensive variation in cell spacing, particularly in between cell trains, could be detrimental to the overall encapsulation efficiency. Progressive draining with a serial drainage junction holds a great potential to further improve the uniformity of cell-cell spacing. Different from other passive techniques such as inertial microfluidics, the 1-1-1 encapsulation platform presented here does not rely on the intrinsic properties of cells, such as cell size, concentration, and stiffness, or rheology of fluids to attain improvement of co-encapsulation efficiency. Therefore, the platform minimizes the dependency on the properties of cells and fluids without compromising throughput, versatility, and simplicity of the encapsulation of cell pairs in droplets. This simple, passive, and promising 1-1-1 co-encapsulation platform has the potential for a broader range of applications in single-cell or cell pairing analysis and is compatible with barcoded-based genomic analysis.

CHAPTER 3: Effects of single-cell morphological properties on their translational and rotational dynamics inside shear-induced droplet microvortices

3.1   Introduction

Droplet microfluidics offers unique and powerful advantages in the development of analytical tools that facilitates single-cell analysis [62]. With water-in-oil droplets serving as micro-reactors, high-throughput profiling of a clonal population of cells is enabled to reveal cellular heterogeneity[63]. A plethora of evidence has shown that the cellular heterogeneity within a clonal population plays a significant role in drug discovery, particularly in the emerging field of cancer immunotherapy [6]. The miniaturization and parallelization of cell processing platforms led to the development of single-cell analysis for diverse biological applications, including genomic and proteomic sequencing methods, antibody discovery, and cell-cell signaling pathways [64–67]. In addition, the compartmentalization of single cell in picoliter-scale droplets leads to improvement in signal-to-noise ratio, detection sensitivity of cell secretions at single-cell resolutions, and multimodal cell-cell interaction studies, whereas the conventional bulk analysis method suffers from obtaining only the averaged response of a cell population and increased background noise from a shared environment.

Various microfluidic platforms have been devised to employ trapping arrays and micro-wells to achieve compartmentalization of a single-cell or cell pair [62, 68–71]. Despite these ingenious designs, these platforms often impose physical constraints and immobility on cells that result in their inability to recapitulate the dynamic physiological microenvironments. Despite some trapping arrays and micro-wells could achieve sealed compartments at the expense of additional loading process, most of the single-cell trapping array and microwells without sealing suffer the risk of false-positive measurements for secretion analysis due to its intrinsic shared microenvironment [68, 72–74]. Thus, droplet microfluidic platform presents distinctive advantage of preserving cellular motility while preventing cross contamination from neighboring cells of interest.

While the droplet generation for cell compartmentalization is a high throughput process on the orders of thousands of droplets per second, the subsequent downstream analysis of each cell-laden droplet is limited due to the complexity of manipulating the encapsulated cells[21]. Downstream analysis of droplet microfluidics often involves affinity-labeling or co-encapsulation of fluorescent beads as reporters, which is restricted to only end-point analyses [75]. The lack of ability to modulate cells within droplets hinders the capacity of droplet microfluidics for complex cellular analysis and dynamic monitoring of cells. Various techniques that involve dielectrophoresis or magnetophoresis have been developed to achieve manipulation of encapsulated cells [76]. However, these active elements introduce complexity of device fabrication and reduced analysis throughput. Therefore, a label-free technique to interrogate the encapsulated cells in droplets would further enhance the capability of droplet microfluidics for single-cell analyses.

The fluid dynamics of moving water-in-oil droplets has been reported by several groups in recent years [77–79]. These studies utilized microscopic particle image velocimetry and computer simulation to study the internal flow field of aqueous droplets in a straight and winding channel through viscous traction at the liquid-liquid interface, which generates a rotational flow field inside the droplet. The resulting internal microvortices in droplet could be applied to enhance mixing in moving droplets.

With absence of perturbation from external active elements, the motion dynamics of an encapsulated cell is predominantly subjected to the flow field of aqueous phase. While a droplet is traversing through a straight channel, a pair of symmetrical microvortices flow field emerges inside the droplet that drives the encapsulated cells to exhibit a significant effect on cell motion dynamics, where a cell exhibits translational or rotational movement. Investigation of moving cell-laden droplets often presents great challenges due to limited field of view and hinders the breadth of analysis. A static array for droplet trapping enables long-term observation of droplets by capturing droplets through hydrodynamics [80], density-difference [81], pneumatic valve [82], electrophoresis

[83], or magnetophoresis [84]. Although a number of strategies have been devised, a stationary cell-laden droplet would be inadequate as the flow fields of internal and external phase are stagnant, inhibiting the study of cell motion dynamics subjected to microvortices inside a droplet. Thus, we developed a new droplet trapping array device that does not only immobilizing cell-laden droplets within the field of view of a camera, but also retaining the ability to generate microvortices inside the droplets by a continuous flow of oil phase.

To accomplish this, we developed a microfluidic droplet trapping array that enables to trap nearly four hundred droplets and simultaneously be modulated by the oil flow. In this study, we investigate shear-induced microvortices in stationary droplets driven by continuous external oil phase to modulate the translational and rotational dynamics of encapsulated cells. To our knowledge, this is the first report on the fluid dynamics of cells inside stationary droplets and the effect of cellular morphological properties in determining their motion in droplets.

Using our droplet trapping array, we demonstrated that the dynamic motion of cells in droplet microvortices is sensitive to the size ratio of cell to droplet, the cell stiffness, and the external phase fluid velocity. We further analyzed the hydrodynamic forces experienced by particles through theoretical and numerical simulations to deconvolute the effects of different physical variables on droplet recirculation dynamics. Finally, we showed that the latrunculin A treated cells, which disrupt microfilament organization for reducing cell rigidity, exhibited rotational motion that localized in proximity to the center of microvortices as opposed to the wild type. These results suggest that the cellular physical characteristics govern the dynamic motion inside the shear-induced droplet microvortices, which presents a new label-free technique for analyzing single-cell morphological properties in droplets. Our theoretical and experimental results provided insights into the fluid dynamics of trapped droplets with shear-induced microvortices, and offer a new droplet microfluidic platform for label-free analysis of single-cell morphology and temporal cellular dynamic monitoring.

3.2   Materials and Methods

3.2.1   Device Fabrication

The channel geometry was designed in computer-aided design software (AutoCAD) and printed on mylar masks through CAD/Art Services as illustrated in Figure 3 - 1. The droplet trapping array device is fabricated through standard photolithography and soft lithography following a similar procedure as explained in Chapter 2 Section 2.2.2   Device Fabrication to achieve a channel height of 40 μm.
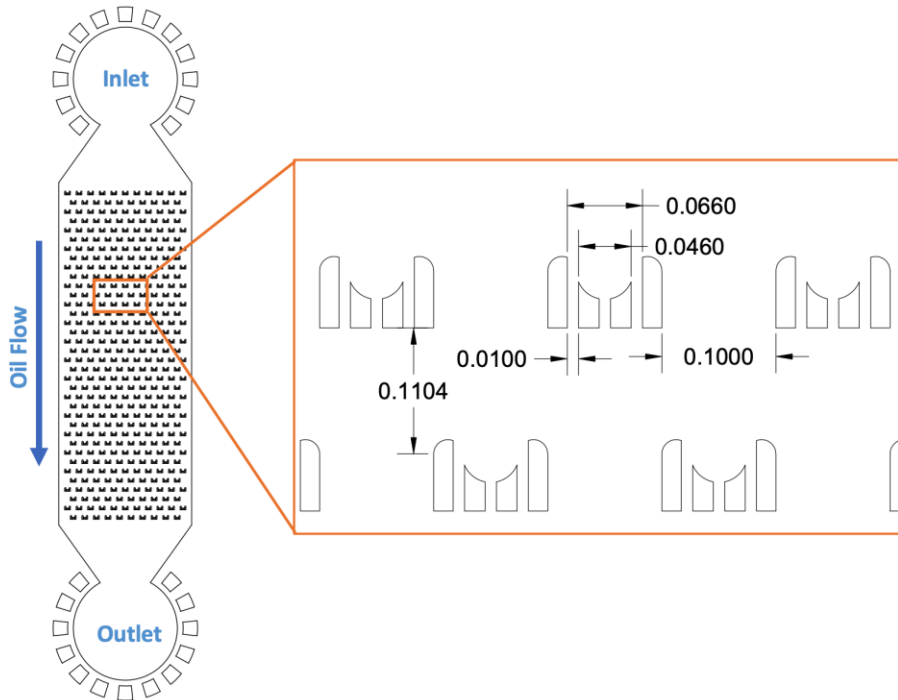
Figure 3 - 1 AutoCAD drawing and channel dimension specifications for the droplet trapping array device*. The labeled dimensions are measured in the unit of millimete*r.

3.2.2   Cell Culture and Latrunculin A Treatment

Human erythromyeloblastoid leukemia cells K562 and Jurkat Clone E6-1 T lymphoblasts (American Type Culture Collection (ATCC)) were used to assess the cell motion dynamics in the droplet microvortices. K562 and Jurkat cells were respectively cultured in a

T-75 cell culture flask using RPMI 1640 medium (Gibco) supplemented with 10% (v/v) fetal bovine serum (Gibco), and 100 U/mL penicillin-streptomycin (Gibco). The cells were cultured in a condition of 5% CO_2 humidified incubator at 37 ºC and passaged every 2-3 days with a seeding density of 1×10^6 cells/mL. In preparation for encapsulation in droplets, the aqueous phase solution was prepared in RPMI medium supplemented with 16% Optiprep, 1% BSA, 0.01% Triton X-100, and 10 U/mL of DNase I. Before the experiment, cells were retrieved and resuspended in aqueous phase solution at a density of 1×10^7 cells/mL.

Latrunculin A (ThermoFisher) is cell-permeant macrolides and toxin that is derived from sponges and nudibranchs. Latrunculin A disrupts microfilament polymerization of cells by binding to monomeric G-actin. This toxin was used to change the morphology of cells, such as surface roughness and compliance, for investigating cell motion dynamics in the microvortices inside droplets. Jurkat cells were selected for Latrunculin treatment by incubating with Latrunculin A at 0.1 µg/mL for one hour. The treated cells were washed with cell culture media and resuspended in aqueous phase solution for encapsulation in droplets.

3.2.3 *Experimental Setup*

Cells were initially encapsulated in droplets prior loading into the trapping array. The droplet generation device from Chapter 2 was used for cell encapsulation that generates homogenous droplets with a diameter of 50 µm. The HFE 7500 supplemented with 2% 008-FluoroSurfactant (Ran Biotechnologies) was used as continuous phase for the droplet generation. Cell suspension and oil were separately loaded into the droplet generation device using two 1 mL plastic syringes (BD, Breda, Netherlands) and were connected to their respective inlets with PTFE tubing (Cole Parmer, ID 0.022 inch and OD 0.042 inch). Lastly,

PTFE tubing was connected to the outlet for collecting droplets into the Eppendorf tube. Both the dispersed phase and the continuous phase were delivered into the microfluidic device at constant volumetric flow rate and individually controlled by syringe pump (Pico Plus; Harvard Apparatus, Inc., MA, USA). The flow rate of the continuous oil phase was set at 5 µL/min, and the dispersed aqueous phase for cell was set at 4 µL/min.

The droplets were subsequently loaded into the droplet trapping array device, as shown in Figure 3 - 2, where the device was mounted onto the stage of microscope for monitoring. A P1000 pipette tip was inserted into the inlet and served as a reservoir for loading droplets and oil. A 3 mL plastic syringe (BD, Breda, Netherlands) was pre-filled with continuous oil phase and connected to the outlet of the trapping array device via PTFE tubing. The pre-filling of oil in syringe and tubing is essential for preventing any gas contraction or expansion to ensure constant flow rate during withdrawal process. Priming of the continuous oil phase into the device would be needed to eliminate any trapping of gas bubbles. The syringe pump was set at any desired withdrawal flow rate up to 20 µL/min. Lastly, the collected cell-laden droplets were transferred by pipetting into the reservoir. Due to the density difference of aqueous and oil phase, the aqueous droplets would float on top. Once the reservoir was almost depleted as the droplets were delivered into the device, addition of HFE 7500 oil (3M) without any addition of surfactant into the reservoir is needed for perfusing oil flow to induce generation of microvortices in droplets.
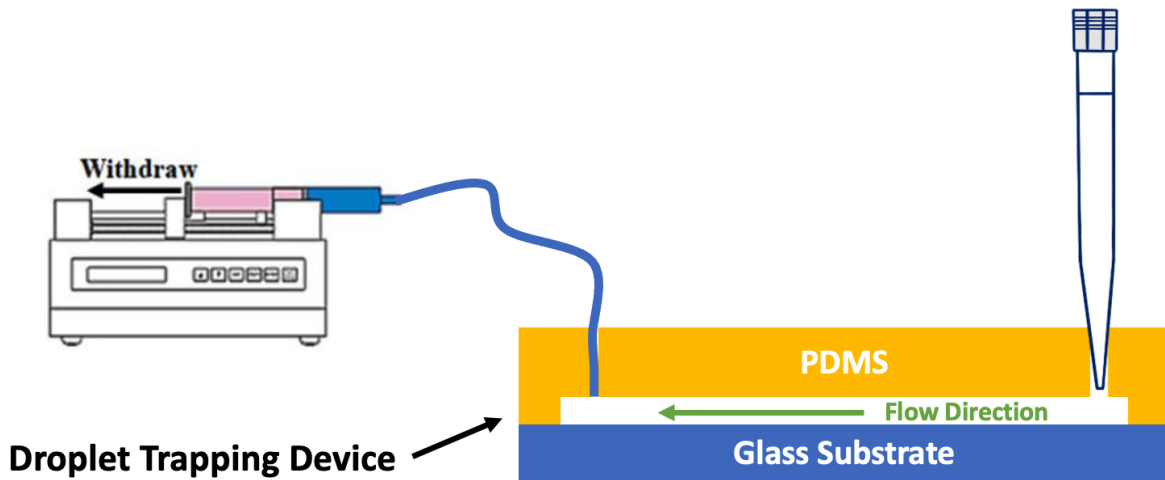
Figure 3 - 2 The experimental setup for droplet trapping array loading. The P1000 pipette tip was inserted into the inlet and served as a reservoir for droplets and oil. The flow was driven by a syringe pump with withdrawal mode to apply negative pressure at the outlet.

3.2.4 Particle Image Velocimetry for Determination of Cell Spinning Rate

Particle Image Velocimetry (PIV) was used to measure the rate at which cells rotated on their axis. Briefly, 300x300 video files with 300 frames acquired at 71 frames per second of cells rotating cells were analyzed using PIVlab 2.61 in Matlab. An interrogation window of 32 px at a step of 16 px was used at pass 1, followed by an interrogation window of 16 px and a step of 8 px for pass 2. To reduce noise in the obtained the velocity and vorticity fields, the complete 300 frames were averaged. Results were overlayed with the grayscale first frame of each video, and were mixed at a ratio of 40% (velocity/vorticity pseudocolor plot) and 60% (grayscale image).

3.2.5 Particle Tracking Velocimetry

To determine the time-dependent position, velocity, acceleration, centripetal acceleration, radius of curvature, and centripetal force of orbiting microparticles, Particle

Tracking Velocimetry was used. Polystyrene microparticles of 1.0 μm (FluoSpheres™, Invitrogen™, USA) and 5.0 μm (Spherotech, USA) were encapsuled inside 50 μm droplets (projected diameter in 40 μm in height device) and flown inside the microfluidic trap array. Particles were then manually tracked to determine their position vs. time. Videos of 1920x1080 in size were recorded for this set of experiments, at a frame rate of 29.97 Hz. All the above-mentioned dynamic metrics were calculated using these measurements and assuming a density of $\rho_p = 1055$ kg m^{-3}. To modify the travelling trajectory and the orbiting velocity of particles, flow rates were parametrically swept from 5 - 20 μL min^{-1}, in 5 μL min^{-1} increments. In addition to microparticle videos, the trajectory of Jurkat and K562 cells in small orbits or spinning mode were acquired using an automated Matlab routine. Videos of cells were recorded using the conventional widefield in an inverted microscope (Olympus IX83, USA).

3.2.6   *Cell Granularity Measurements from Videos*

Self-rotation videos of single encapsulated cells provided multiple images where granularity was measured. The size of granules (high white pixel intensity regions) were determined by analysis of widefield imaging of K562 cells, followed by application of an automated Matlab imaging analysis routine based on the edge detection algorithm available from the help center (*Detect Cell Using Edge Detection and Morphology*).

3.3   Results and Discussion

3.3.1   Design Concept of Droplet Trapping Device for Induced Microvortices

Our microfluidic droplet trapping array device consists of one inlet and outlet with a chamber of 378 droplet traps (Figure 3 - 3a). As depicted schematically in Figure 3 - 3b, each droplet trap is composed of four pillars separating in 10μm gap, in which the middle two pillars are shorter relative to the outer pillars to create a pocket for droplet trapping. Once a droplet is docked into the trap, the obstruction of the middle gap increases the resistance that diverts the subsequent droplets to flow over into the next row of traps. As a result, we could achieve 100% single droplet occupancy in the trapping array chamber (Fluorescent microscopy image: Figure 3 - 3c and d; Bright-field microscopy image: Figure 3 - 4).

The internal flow field of a moving droplet is induced because of the viscous shear stress is being exerted along the liquid-liquid interface by the external oil phase. To enable this shear stress at the interfacial surface of a stationary droplet, the two outer gaps of the trap serve as bypass channels that enable oil phase to flow around the droplets (Figure 3 - 3e). Particularly, the droplet trapping chamber is specially designed to have a height of 40 μm in order to flatten a 50 μm diameter droplet to exhibit a puck-like shape. Thus, the top and bottom of a droplet are in contact with the microfluidic channel walls once loaded, while the two lateral sides of a droplet would be the only sides that are exposed to the continuous flow of oil phase. With the continuous flow of oil phase exerting viscous shear stress predominantly on both sides of a droplet, a pair of symmetrical two-dimensional microvortices is induced in left and right halves of a droplet with respect to the oil flow direction (Figure 3 - 3f).

In addition, as the trapped droplet blocks the central slit between middle two pillars of the trap, which the oil flow is directed into the bypass channels, resulting a fraction of the droplet does not experience shear stress due to its contact with the pillars (Figure 3 - 3g). Thus, the primary microvortices in droplet induced by the continuous oil flow create a pair of smaller secondary microvortices (Figure 3 - 3h). In comparison to the microvortices in a moving droplet, the shape of these primary microvortices in stationary droplet exhibits distinctive resemblance to the ones observed in a moving droplet. Thus, this droplet trapping does not only offer exceptional trapping efficiency to attain stationary droplets for monitoring within the field of view, but also preserving the characteristics of internal microvortex dynamics of a droplet.

By exploiting the ability of controlling microvortices inside of stationary droplets through modulating the flow rate of oil phase, the simplicity and scalability of our trap design offers unprecedented capability in droplet microfluidics for single-cell or immune cell-cell interaction studies. While these stationary droplets enable longitudinal observation of flow pattern and the encapsulated cells, this device also offers dynamic manipulation and dynamic force exertion on the encapsulated cells for biomechanical analysis at scale.
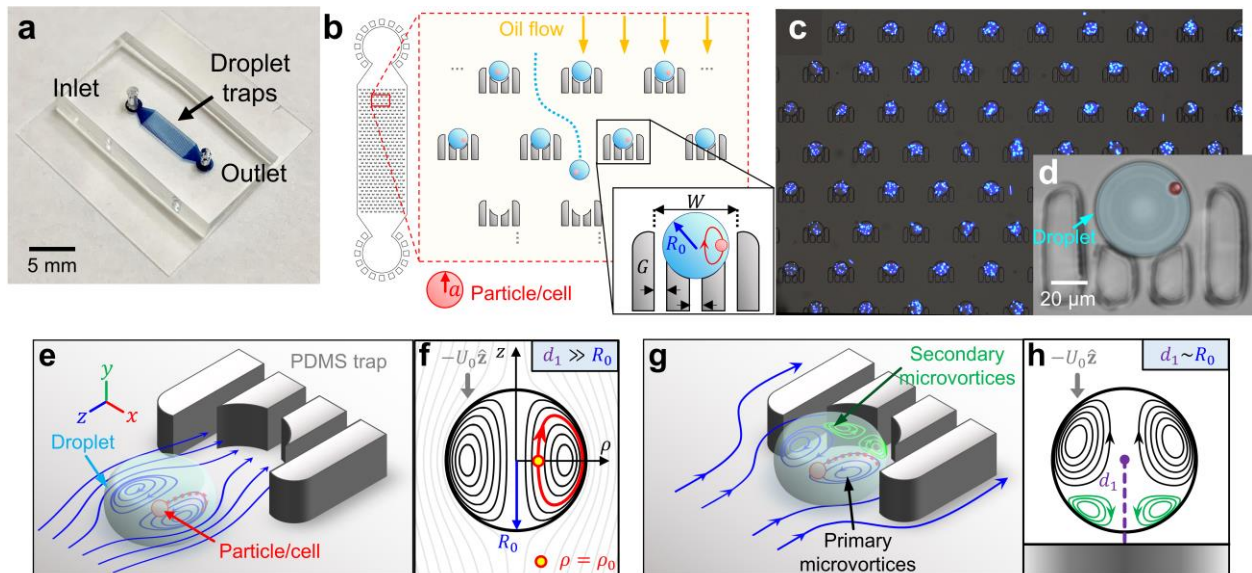
Figure 3 - 3 a) Microfluidic trap device for controlled droplet microvortex generation at scale. b) Device schematic, illustrating the loading of cell-laden droplets into traps. c) Fluorescence microscopy image demonstrating 100% efficiency droplet trapping. Trapped droplets were loaded with 1 μm fluorescent beads for visualization. d) Blow-up of a single microfluidic trap, with a droplet containing a 5 μm bead inside. The device has a wo-step droplet trapping mechanism: 1) Before reaching an individual trap, viscous shear on the surface of moving droplets generates two nearly symmetric primary microvortices inside them (e,f). 2) Droplets are then stopped by blocking the central slit of the trap (g). Primary and secondary vortices are then formed inside the immobilized droplet due to their proximity to PDMS walls (g,h).
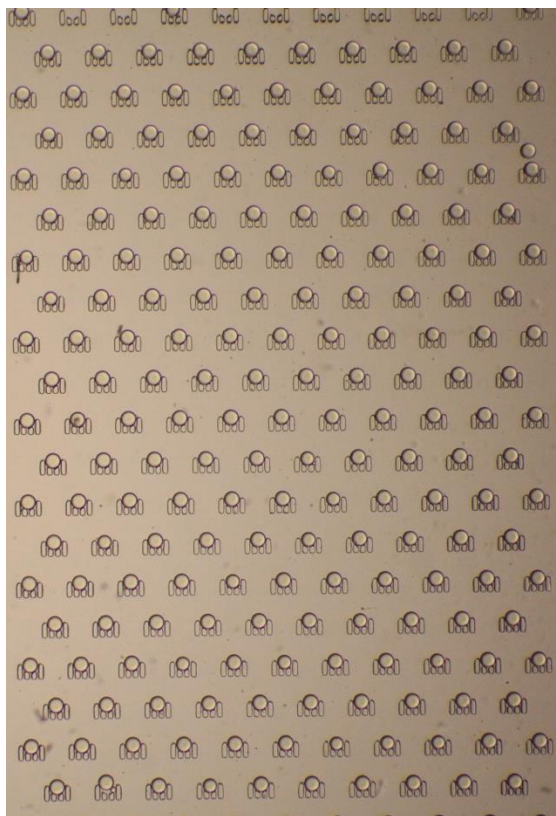
Figure 3 - 4 Bright-field microscopy image demonstrating 100% efficiency of droplet trapping.

3.3.2   Droplet Shrinkage Analysis

While the droplets are docked into the trapping array device and subjected to a

continuously flowing of oil phase, a significant shrinking in droplet size is observed. For

troubleshooting and extending the shrinking time, different concentration of 008-

FluoroSurfactant was used to investigate the rate of droplet shrinkage, ranging from 0, 1,

and 2% FluoroSurfactant in HFE 7500 oil. For one hour of oil perfusion at a flow rate of 3

µL/min, bright-field image was acquired at a five-minute interval, and their respective

droplet size was measured in ImageJ. The timelapse image of each condition is shown in

Figure 3 - 5, where there was a significant change in droplet size after one hour of oil

perfusion with 2% surfactant. However, the droplet shrinking rates for the testing group 0

and 1% surfactant are relatively similar under the oil flow rate of 3 µL/min, as illustrated in

47

Figure 3 - 6a. Under the HFE 7500 with 2% surfactant, the droplet diameter decreased below half of its original size after 55 minutes, whereas the droplets reached 80% of their original size for using oil with 0 or 1% surfactant. Furthermore, Figure 3 - 6b demonstrated the droplet shrinkage for flowing oil with different surfactant at a higher flow rate at 9 μL/min. We observed that there was a significant decrease in droplet diameters for all three conditions tested, where the group with 2% surfactant showed the highest decreased in droplet size and the groups with 0 and 1% surfactant were similar. The faster rate of droplet size decreased at higher flow rate suggested that the formation of nanometer-scale droplet due to higher shear stress exerted at the liquid-liquid interface by the continuous oil flow.

In addition to the investigation of different surfactant concentrations in oil, we continued our effort to further reduce the droplet shrinkage for extended period of time. Due to the intrinsic properties of PDMS, this material is gas-permeable and known for sample evaporation, especially in the aspect of microfluidics due to high surface-to-volume ratio. Despite the PDMS is hydrophobic, sample evaporation is also another factor that is attributed to the droplet shrinkage. A study has shown that the use of Parylene AF4 coating on microfluidic channels would further mitigate the droplet shrinkage due to its enhanced hydrophobicity of PDMS channels [85]. Thus, we used another variant of Parylene, called Parylene C, which also exhibits strong hydrophobicity for our droplet shrinkage analysis. Our droplet trapping device was coated with Parylene C through standard vapor deposition method. The results suggested that there was a slight improvement on the rate of droplet shrinking by using the Parylene C coated device (Figure 3 - 7 and Figure 3 - 8). There was less than 20% decreased of its original droplet size for the Parylene C coated device, which

showed 5% improvement in comparison to the non-coated device. Therefore, Parylene C coated device would be recommended for long term on-chip droplet analysis to prevent sample evaporation.
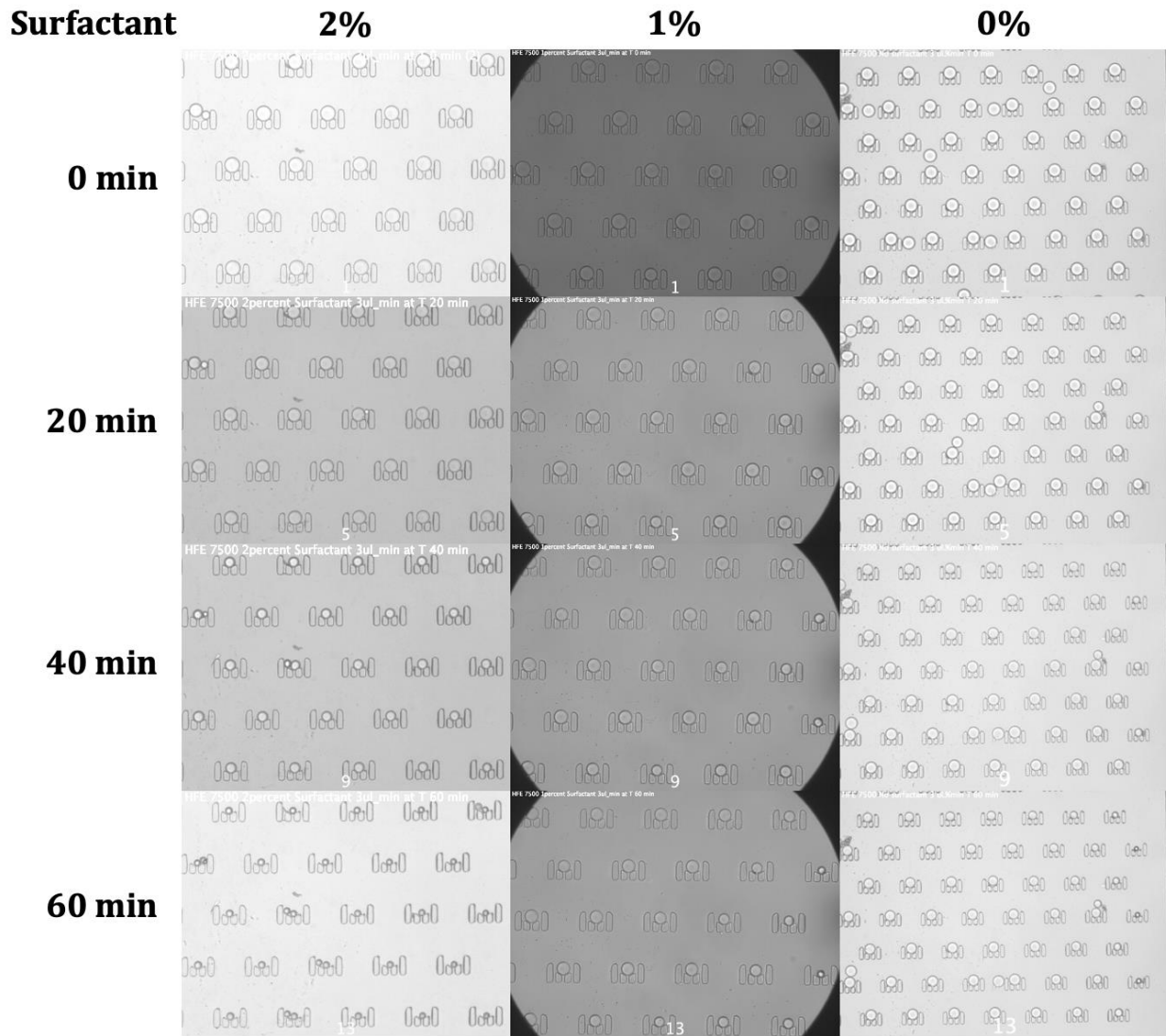
Figure 3 - 5 Timelapse images for droplet shrinkage analysis under different surfactant concentration in HFE 7500 oil flowing at 3 μL/min.
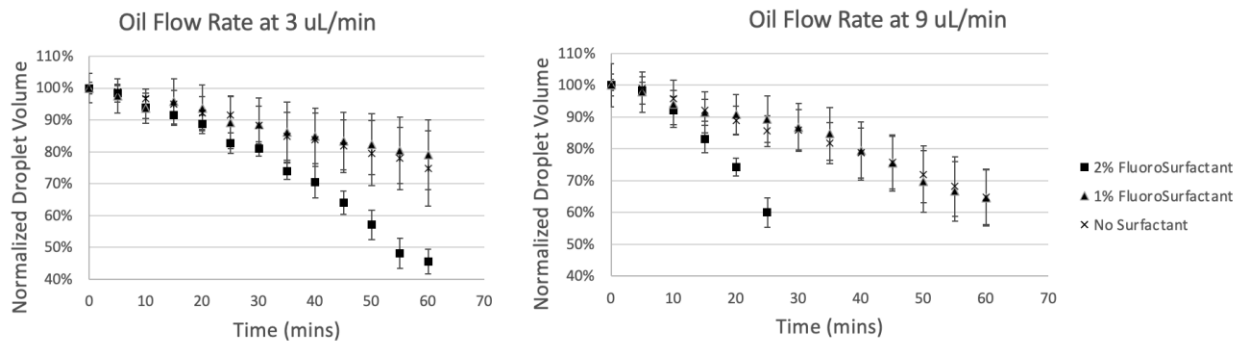
Figure 3 - 6 Normalized droplet size shrinkage for one hour of oil perfusion under different flow rates and surfactant concentration.
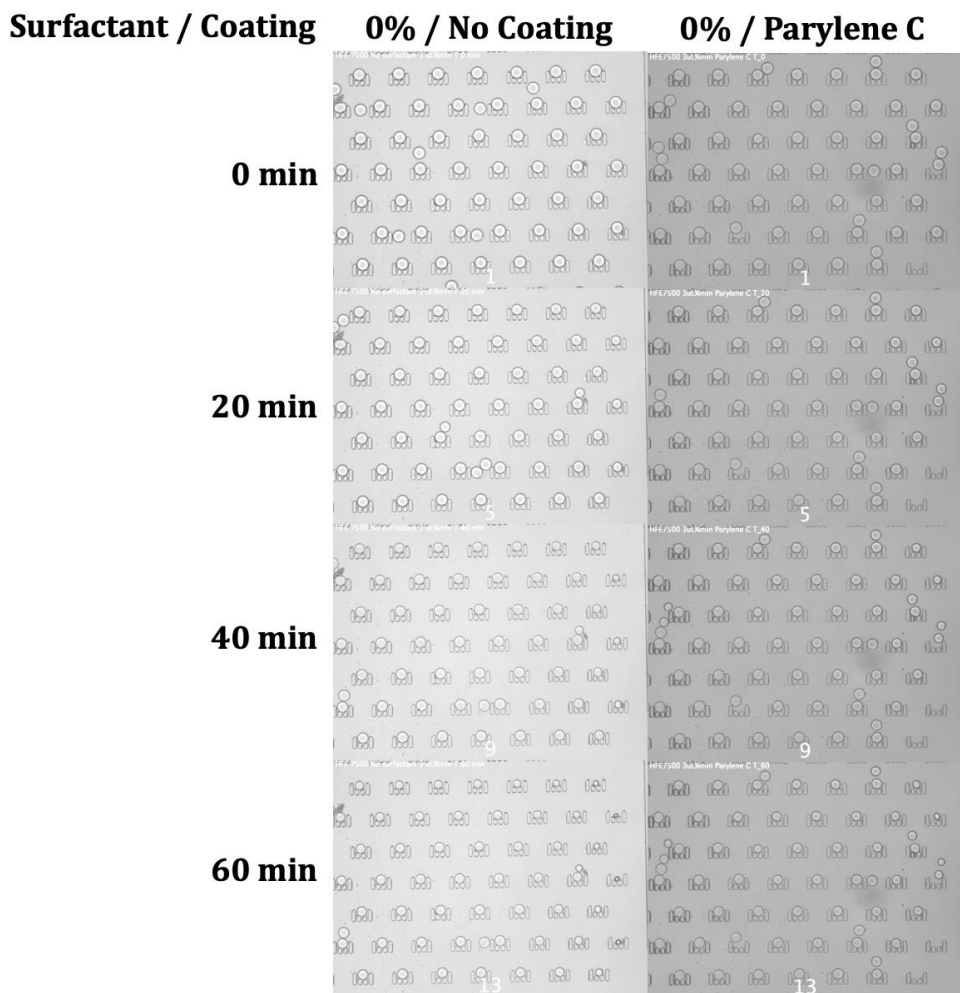
Figure 3 - 7 Timelapse images for droplet shrinkage analysis using Parylene C coated and non-coated droplet trapping device in HFE 7500 oil flowing at 3 μL/min.

Oil Flow Rate at 3 uL/min
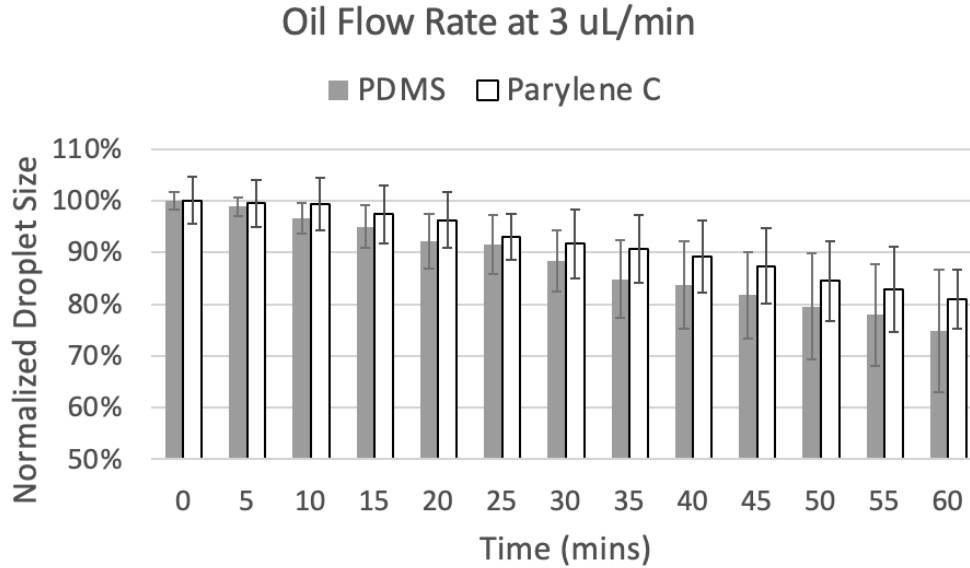
Figure 3 - 8 Histogram for the performance of preventing droplet shrinking using non-coated and Parylene C coated droplet trapping device.

3.3.3   *Theoretical Cell Orbiting Period in Droplets*

The simplest theoretical model that captures the minimal elements to represent inner droplet flow in 3D is that of an inner phase static spherical droplet of radius R_0 and dynamic viscosity η_i, submerged in a continuous outer phase of dynamic viscosity η_o that flows at uniform velocity U_0 far from the fixed sphere. Under these conditions, the droplet will experience shear-stress that results in inner (u^i) and outer (u^o) flow velocity fields. Assuming a laminar, inertia-less flow and neglecting surface tension gradients, both fields admit analytical representations that are known as Hadamard-Rybczynski velocity fields. [86] These velocity fields, although idealized, describe some of the functional relationships between quantities of interest with the physical parameters of the problem, and thus facilitates the study of inner droplet flow. The left side of Figure 3 - 3f illustrates the Hadamard-Rybczynski velocity field streamlines as the outer phase with velocity $-U_0\,\hat{\mathbf{z}}$

flows past the sphere. Under these conditions, the inside velocity field can be fully represented with radial and angular components in spherical coordinates, $u^i = (u_\rho^i, u_\theta^i)$:

$$u_\rho^i(\rho, \theta) = \frac{R_0}{\tau} \cos\theta \left[\left(\frac{\rho}{R_0}\right)^2 - 1 \right], \qquad\qquad \text{(Eqn. 3.1a)}$$

$$u_\theta^i(r, \theta) = \frac{R_0}{\tau} \sin\theta \left[2\left(\frac{\rho}{R_0}\right)^2 - 1 \right], \qquad\qquad \text{(Eqn. 3.1b)}$$

where a characteristic timescale τ has been identified:

$$\tau = \frac{2R_0}{U_0}(1 + q), \quad q = \frac{\eta_i}{\eta_o}. \qquad\qquad \text{(Eqn. 3.2)}$$

Hadamard-Rybczynski velocity streamlines inside the inner phase describe a family of Bernoullian quartic curves which admit the following parametric equation representation:

$$\frac{\rho_0}{\rho}\sqrt{\frac{\rho_0^2 - R_0^2}{\rho^2 - R_0^2}} = \sin(\theta), \qquad\qquad \text{(Eqn. 3.3)}$$

where ρ_0 is the starting radial defining a specific closed quartic curve (see Figure 3 - 3f, left). Ideally small particles recirculate these closed pathlines, thereby describing a periodic motion on both $\rho(t)$ and $\theta(t)$ coordinates. This orbiting period, T_{orbit}, can be obtained by solving a system of ordinary differential equations that are defined by the radial and angular components of the velocity field (Eqns. 3.1a,b). We found that the solution to this system of nonlinear differential equations can be written in the implicit form:

$$t - t_0 = \tau \int_{\rho_0}^{\rho} \frac{R_0 \rho' d\rho'}{\sqrt{(\rho'^2 - R_0^2)(\rho'^2 - \rho_0^2)(\rho'^2 + \rho_0^2 - R_0^2)}} \qquad \textit{(Eqn. 3.4)}$$

where $\rho(t_0) = \rho_0$ set as the start point of the particle path, and the time constant τ is given by eq. (3.2). From eq. (3.4), the recirculation time or cell/particle orbiting period can be readily computed as:

$$T_{orbit} = \frac{2\tau}{\sqrt{(\rho_0/R_0)^2 - 1}} \left[K\left(\frac{\rho_0^2}{R_0^2 - \rho_0^2}\right) - F\left(\phi, \frac{\rho_0^2}{R_0^2 - \rho_0^2}\right) \right] = \tau f(\rho_0, R_0), \qquad \textit{(Eqn. 3.5)}$$

where ρ_0 is the vortex starting point, $K(m)$ and $F(\phi, m)$ are the complete and incomplete elliptic integrals of the first kind, respectively, with $\phi = \sin^{-1}[(R_0^2 - \rho_0^2)/\rho_0^2]$ and $m = \frac{\rho_0^2}{R_0^2 - \rho_0^2}$. Although being an implicit solution to the particle equations of motion, eq. (3.5) can be directly used to compute particle trajectories.

3.3.4   Characterization of Cell Dynamic Motion in Stationary Droplets

The ability to controllably modulate the encapsulated cell in droplets with the use of only oil flow is powerful and holds the potential to greatly impact many cellular biomechanics applications. In this section, we deconvolute the roles of outer oil flow conditions to modify inner droplet flow dynamics that results in cells to exhibits translational and rotational (orbiting and spinning) motion within the microvortices.

It was experimentally observed that encapsulated objects inside trapped droplets tend to recirculate due to the constant hydrodynamic shear that is impinging on the front

part of droplets (Figure 3 - 3e-h). This source of momentum is transmitted into the droplet fluid, and eventually recirculating objects find a stable, steady-state path, which can be recognized as a limit cycle resembling a slightly modified Bernoullian quartic cuve. We hypothesized that particle size would affect the trajectory of encapsulated objects, owing to the different hydrodynamic forces that would act on larger particles. Particles and cells of different sizes were therefore tested to see the effect that particle size to droplet size ratio ($\phi = a/R_0$) had on the trajectory and temporal dynamics of their limit cycle. As seen in Figure 3 - 9, larger objects were subject to smaller recirculation paths, as measured by the percent orbit area. The normalized orbit area has been defined as as the percent ratio of the projected area in the direction of the optical axis of observation of the steady-state orbit described by the travelling object, to the projected area of half a droplet, $A = \pi R_0^2/2$. An orbit area percent of 100% therefore represents a theoretical upper bound where a particle travels on a loop as large as half the droplet circular area $-$ a limit seldom reached by circulating particles inside well-centered droplets under all conditions here tested. Similarly to polystyrene beads, cells of different sizes (Jurkat, with radius a = 5.0±0.5 μm , and K562, a = 6.9±0.7 μm) exhibited a noticeable change in orbit area, with ∼3.93% and 0.08% for Jurkat and K562 cells, respectively.

It was determined that for those particles or cells that display orbit areas smaller than the area of the particle itself, the dynamic behavior is better described as spinning – if not a combination of the two dynamic modes. This relationship has been illustrated in the form of an area function of the particle to droplet size ratio ϕ (Figure 3 - 9, dashed line). For the cell lines here tested, because of their size ratio with respect to the length scale of the droplet, we predominantly observed spinning motion at flow rates of 20 μL min^{-1} (in a later section,

however, it will be showed that flow rate also played an important role in defining orbiting vs. spinning).

Orbiting Regime

To quantify the dynamics of the orbiting regime, we recorded footage of fluorescent beads recirculating inside stationary, trapped droplets under different flow conditions. Figure 3 - 10a-i portrays a circulating fluorescent 1.0 μm particle inside a droplet. A dashed cutline illustrates the temporal dynamics exhibited by the recirculating bead, clearly demonstrating a reproducible periodic orbiting path. In Figure 3 - 10a-ii, Particle Tracking Velocimetry (PTV) measurements of an actual recirculating particle are shown with respect to the projected circular area described by the droplet, while Figure 3 - 10a-iii displays the corresponding time tracks of the polar and angular position of the particle (with respect to the droplet center). Fourier functional fits using only two harmonics demonstrate that the orbiting phenomena has a strong periodicity.

We next examined the effect of flow rate Q on the recirculation time (or orbiting period T_{orbit}). By controlling the externally applied flow using a syringe pump, we observed that T_{orbit} inversely decreased with flow velocity (see Figure 3 - 10a-iv). Fourier analysis of the track data (e.g. Figure 3 - 10a-iii) allowed the direct and automated measurement of the recirculation time for each flowrate by identifying the first peak of the Fourier transform spectrum of $\rho(t)$ after removal of the "DC" component of the signal (Figure 3 - 10a-v). The time reduction behavior can be successfully explained by eq. (3.5), where recirculation time is seen to depend directly on timescale τ, which itself is inversely proportional to the far-field uniform flow velocity U_0 in the ideal spherical droplet case. Assuming the outer flow velocity

U_0 is constant outside stationary cell-laden droplets, and neglecting the third dimension in the problem (shallow channel approximation), we conclude that eqs. (3.2) and (3.5) can be used to fit the experimentally measured T_{orbit} times. Furthermore, because the external flow speed U_0 appears in eq. (3.2), rather than fitting to the the externally applied flow rate, a functional fit was performed against Q, justified by the fact that for Stokes flow, $U_0 \sim \alpha Q$. The R^2 value of 0.996 supports the hypothesis that Hadamard-Rybczynski-like vortices with Bernoullian quartic curve shape arise in the stationary droplets.

Spinning Regime

To quantify the temporal dynamics of cells in spinning regime, rather than performing single particle PTV, we performed PIV. In this case, PIV measurements provide a measurement of the video footage pixel flow dynamics (in pixels/frame), rather than an explicit particle velocimetry. By quantifying pixel movement in this way, the velocity of feature motion in footage could be determined after calibration. Figure 3 - 10b-i shows an encapsulated K562 cell, which by virtue of its particle size to droplet ratio falls on the spinning regime. Moreover, Figure 3 - 10b-ii illustrates velocity measurements for the self-rotating cell. In parallelism to the PTV measurements demonstrating periodicity in the orbiting regime, vorticity calculations of the pixel flow field enable direct measurement of the pixel flow angular velocity, as seen in Figure 3 - 10b-iii.

Because cells were subject to self-spinning at a specific Euler angle, continuous recording of different facets of single-cell was possible. Operation in the spinning regime therefore allowed single-cell morphological inspection via transmitted light wide-field microscopy at 360° angles. Enabled by the self-spinning mechanism of our cell-laden droplet

trap microdevice, we recorded K562 human erythroleukemia cells at different view angles (Figure 3 - 10b-iv). K562 cells can contain various types of granules, including CD63+ lysosomal granules.[87] Using an automated edge detection routine, we measured the average granule size per frame of video, and plotted it against the video timestamp in Figure 3 - 10b-v. As expected, the measured average granule size per inspected frame is periodical over time due to the self-spinning mechanism. As plotted in Figure 3 - 10b-vii, analysis of the Fourier spectrum of the average granule size signal further confirms the self-rotational dynamics of the droplet encapsulated cells. Furthermore, excellent agreement between pixel vorticity (or angular velocity) and the Fourier peaks in Figure 3 - 10b-vii corroborate the periodical dynamics.

Lastly, we employed the described Fourier peak identification procedure to measure periodicity or spinning/rotation time as a function of externally applied flow rate. Although not ideally represented by eq. (3.2), we found that the timescale τ is still applicable to the estimation of single-cell rotation time. This can be explained by the fact that particles with high ϕ values, such as K562 cells in 50 μm droplets, will tend to be spatially confined close to the center of the vortices. At this point, vortices resemble a forced vortex flow field (also referred to as solid body rotation [88]), where $T_{orbit} \rightarrow \sqrt{2}\pi\tau$ as $\rho_0 \rightarrow R_0/\sqrt{2}$ (the vortex center in the ideal case of eq. (3.2)). Because of this, a semi-rigid object will eventually try to match the vorticity of the local flow field, which is inversely proportional τ, or proportional to Q. This behavior was confirmed in a parametric study of flow rate in Figure 3 - 10b-vi, which demonstrates an equivalent functional relationship as that of Figure 3 - 10a-iv. These results point to the generality of cell orbiting and spinning mechanisms inside droplets, which can not only be finely tuned to control the shear field experienced by single cells, but

also be tailored to image and quantify cell texture and morphological features with potential for scalable throughput analysis. This flexibility of analysis is currently non-existent in the microfluidic field, because the available single-cell rotational control methods, such as microcapillary rotation[89] and electric field induced cell electrorotation [90, 91] are inherently not scalable. In addition, microcapillary rotation requires embedding cells in cytotoxic thixotropic index-matched gel, and in electrorotation, solutions are different from normal isotonic media, thus limiting the biological assays that can be conducted during multi-angle observation.
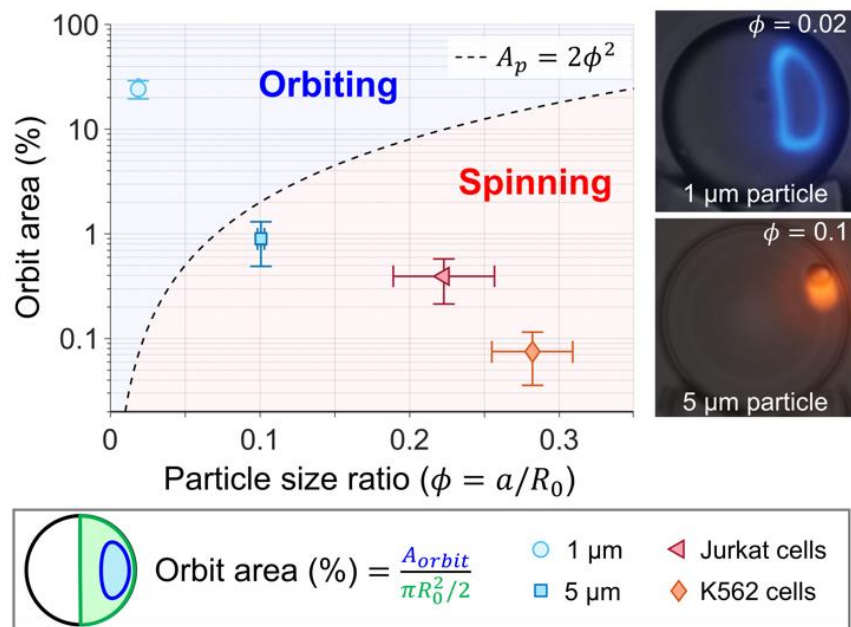
Figure 3 - 9 Effect of particle/cell size to droplet radius ratio on particle dynamics inside trapped microfluidic droplets. Particle dynamics were quantified by the percent area occupied by the travelling path (orbit) described by the encapsulated particle or cell. Two distinct dynamics, namely orbiting and spinning, were observed depending on the size of the particles, as depicted in the inset images.
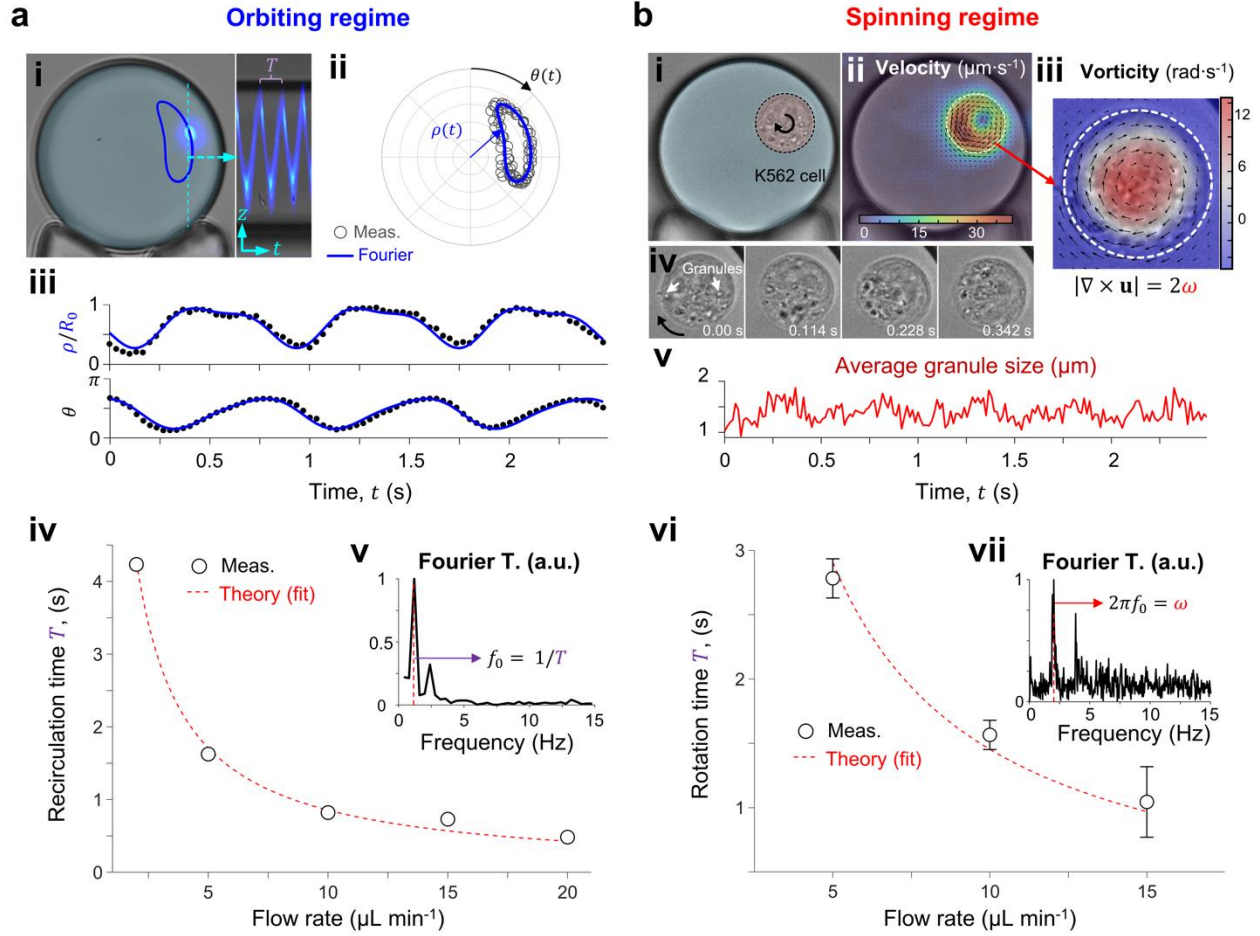
Figure 3 - 10 Size-dependent translational (orbiting) vs. rotational (spinning) dynamics of droplet encapsulated objects. a-i) Fluorescent bead (1 μm) exhibiting orbiting dynamics. Its repeated circulation can be viewed by means of a temporal projection with period T. a-ii,iii) Particle Tracking Velocimetry (PTV) of the particle, showing radial and angular periodicity. a-iv) Recirculation time (period of plots in a-iii) of particles as a function of the externally applied flowrate. a-v) Fourier transform of the radial component of the position vector demonstrates a marked periodicity. b-i) An encapsulated K562 cell self-rotating (spinning) on its axis. b-ii) Particle Image Velocimetry (PIV) was used to illustrate that only pixels belonging to the cell in a frame displayed the highest motion. b-iii) Pixel vorticity measurements obtained from PIV analysis. b-iv) Footage of the spinning K562 cell, portraying different angles as the cell rotates. For each different view angle, a different distribution of observable granules can be measured, the average of which is plotted in a time-series plot in b-v). b-vi) Measured rotation times for K562 cells as s function of the externally applied flow rate. b-vii) Fourier transform of the time-series average granule size data. A sharp peak in the frequency spectrum coincides with the cell spinning frequency, which in turn can be connected to the PIV-measured pixel vorticity of the recorded videos and the K562 rotation times.

3.3.5   Visualization of Internal Flow Field using Microparticles

To enable a visualization of internal flow dynamics inside a trapped droplet, we encapsulated fluorescent microparticles of 1 and 5 μm diameter, respectively, to enable the observation of particle trajectory in trapped droplets under different continuous oil flow conditions, ranging from 5 to 20 μL/min. Fluorescent microscopy image was acquired by setting the exposure time of minimum 5 seconds to see the trajectory of a particle. Figure 3 - 11 indicates the presence of microvortices inside the trapped droplets for 1 μm bead, as it was in the orbiting regime. On the contrary, 5 μm bead was in the spinning regime as it localized in the center of the microvortex for all the oil flow rates tested. Furthermore, we observed that the particles, either in orbiting or spinning regime, converges toward the center of microvortices as the oil flow rate increases. This phenomenon can be attributed to the velocity gradient between the outer and inner microvortex, where the velocity is higher on the outer microvortex. Thus, as the oil flow rate increases, the velocity gradient between the outer and inner microvortex and flow field density increase, resulting a particle to converge into the center of microvortex.
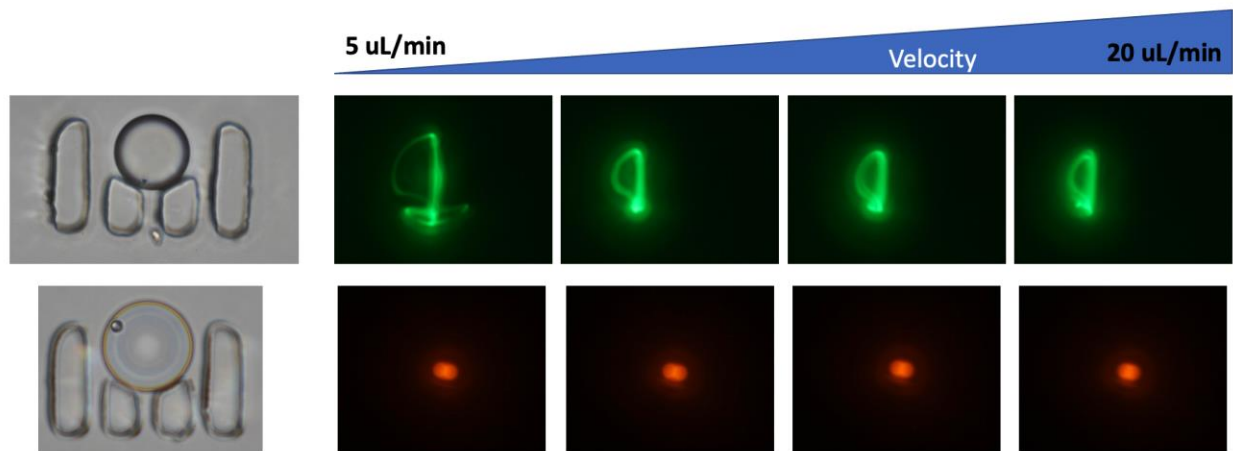
Figure 3 - 11 Visualization of droplet internal flow dynamics using fluorescent microparticles (Green: 1 μm diameter bead and Red: 5 μm diameter bead).

3.3.6   Effects of Cell Morphology on Translational and Rotational Dynamics

To investigate the effect of cell size on the extent of dynamic motion inside the microvortices, two wild type cell lines Jurkat and K562, with nominal cell diameters of 13 and 20 μm respectively, are encapsulated in droplets with 50 μm diameter and subjected to continuous oil flow after immobilized by the trapping array. The trajectory path of the cell is represented with a direct least square fitting of ellipse, in which the elliptical area is normalized against the area of a cell. The normalized orbital areas from both cell types are assessed under oil flow rate of 5, 10, 15, and 20 μL/min (Figure 3 - 12a). Driven by the microvortices, a cell would perform either an orbit or spinning dynamics, which the axle of rotation is outside or inside of a cell respectively. Thus, the normalization of orbital area (NOA) enables differentiating these dynamic motions of a cell by setting the threshold at one, where the orbiting motion has NOA greater than one and the spinning motion has NOA of less than one. At oil flow rate of 5 μL/min, the NOA of Jurkat wild type is found to be above one, which clearly reveals its orbiting motion within a droplet. As oil flow rate increases, the Jurkat wild type NOA decreases and switches into spinning regime. By contrast, despite the reduction of NOAs for K562 wild type with increasing oil flow rate, the K562 cells remain to be in spinning regime for all tested oil flow rates with NOAs that are significantly lower than the NOAs of Jurkat wild type. These data suggest that the ratio of cell size and microvortex size plays a critical role on the motion dynamics. Cell type with larger diameter could reach spinning regime due to the footprint of a cell overlaps the center of a microvortex. Thus, the larger cell type can localize in the center of a microvortex, resulting a significant lower NOA that is less sensitive to the external oil flow rates. On the contrary, Jurkat wild type cells that are smaller in size exhibit a considerable decrease in NOA at higher oil flow rate. At a higher oil flow rate,

the viscous shear exerted at the interfacial surface increases such that the inner aqueous flow rate of a droplet is also greatly increased. At a given flow velocity of a microvortices, a cell would reach an equilibrium position within a microvortex, such that the drag force and the rotation-induced lift force experienced by the cell is balanced. The data indicate that the external flow rate can modulate the motion dynamic of a cell within the microvortices in droplets.

In addition to the effect of cell size, we further investigate the effect of cell stiffness on the extent of dynamic motion inside the droplet microvortices. In comparison to the wild type of Jurkat cell line, we perform Latrunculin A (LatA) treatment to depolymerize the organization of microfilament in Jurkat cells, achieving the disruption of cellular stiffness. The LatA treated Jurkat cells are encapsulated in droplets and subjected to the continuous oil flow field at 5, 10, 15, and 20 μL/min. The NOAs of LatA treated and wild type Jurkat cells are shown in Figure 3 - 12b, where the NOAs of LatA treated cells show a discernable reduction as opposed to the wild type. At the oil flow rate of 5 μL/min, the LatA treated Jurkat cell shows a 58% decrease than the NOA of wild type, which reaches the spinning regime. Particularly, as the oil flow rate increases, the LatA treated cells under the oil flow rates at 15 and 20 μL/min further localize in the microvortex center with 90% decreased of NOAs in comparison to wild type. These data demonstrate a significant difference in NOAs between wild type and LatA treated Jurkat cells at high oil flow rate regime, signifying the effect of cell stiffness on the dynamic motion within the microvortices. Due to the depolymerization of microfilament in a cell, a cell with lower stiffness would be more compliant to the hydrodynamics of microvortices, which facilitates LatA treated cell to localize in the center of microvortices and self-spin. Collectively, the cell motion dynamics within microvortices

that are induced by external oil flow enables a hydrodynamic modulation of the encapsulated cells in droplets. Furthermore, the normalized orbital area is sensitive to differentiate cells with various morphologies, including size and stiffness, which offers a new label-free method to study single-cell biomechanical properties in droplets.
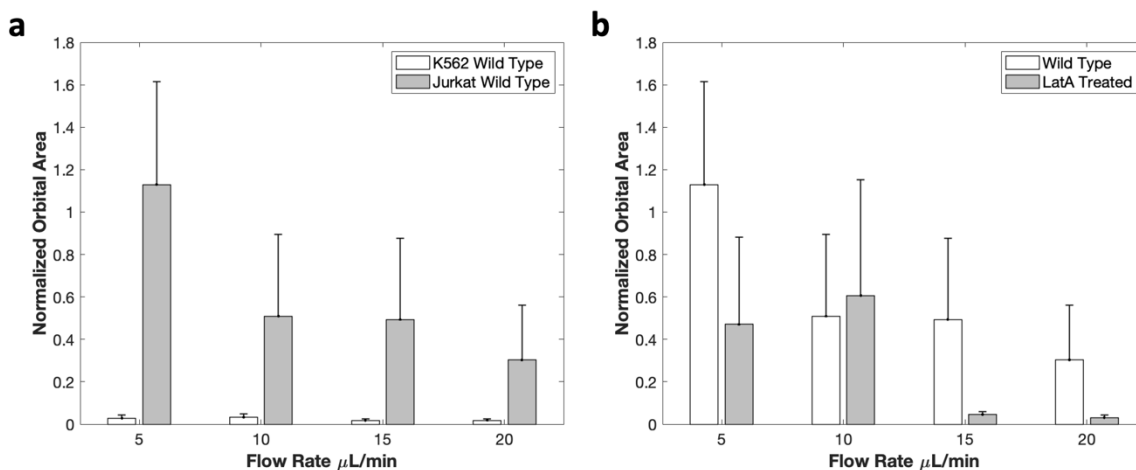
Figure 3 - 12 a) Histogram of the normalized orbital area within a droplet between wild type K562 and Jurkat demonstrates that the effect of cell size on the motion dynamics of cells within the microvortices (N=3). b) Histogram of the normalized orbital area within a droplet between wild type and LatA treated Jurkat cells demonstrates that the effect of cell stiffness on the motion dynamics of cells within the microvortices (N=3).

3.4   Conclusion

Droplet microfluidics has enabled high-throughput single-cell analysis by providing individual micro-reactors. Recent advances enabled trapped single droplets in a high-throughput array to investigate time-dependent single-cell reactions in real time. Therefore, the understanding of hydrodynamic flow properties in droplets is a fundamental requirement in governing the reaction conditions and cellular analysis. Although prior studies have demonstrated that hydrodynamics of water-in-oil emulsion droplets flowing in microfluidic channels, the flow dynamics of trapped or stationary droplets remain largely

unexplored. To address this area, we designed a droplet trapping array device to immobilize cell-laden droplets that would be subject to continuous oil flow to shear-induce microvortices. Using this device, we demonstrated that the inner flow dynamics of a stationary droplet with continuous oil flow consists of two pairs of symmetrical primary and secondary microvortices.

Furthermore, understanding the influence of external oil flow to the water-oil interfacial interaction with inner droplet flow enables setting specific microreactor conditions for individual encapsulated cells in droplets within a large trapping array. While the cell-laden droplets are trapped in our device with continuous oil perfusion, we discovered that the encapsulated cell exhibits two distinctive dynamic motion: orbiting and spinning. With various external oil flow rates tested, we have shown that the recirculation and rotational times have an inverse relationship with external flow velocity, which matches with the analytical model. In addition, the cell motion dynamics within the microvortices in droplet is also a periodic movement. By exploiting the periodicity of a cell movement within microvortices and its high responsiveness to the oil flow rate, our device offers a new capability to modulate the dynamics of encapsulated cells in droplets by simply tuning the external flow rate, instead of the use of any complex equipment such as optical or acoustic tweezers for cell manipulation. This technique further enhances the potential of droplet microfluidic systems for complex biological analysis and cellular monitoring.

In addition to characterization of inner droplet flow dynamics, we decoupled the effect of cell morphology on the extent of cell dynamics in the microvortices that led to translational or rotational motion. Within the microvortices, the size of encapsulated cells with respect to droplet size plays a significant role in defining an orbiting or spinning

64

dynamics. Larger cell would result in spinning motion as the area of a cell overlaps the center of a microvortex in droplet, whereas a smaller cell leads to an orbiting motion as it follows the streamline of a microvortex. More importantly, our platform has shown the ability to discern cell stiffness based on its dynamics within the microvortices. According to the normalized orbital area of a cell in a stationary droplet, we observed a significant reduction in NOA for cell population with lower stiffness. As a result, our platform demonstrated the sensitivity based on NOA to differentiate cells with different morphology.

In summary, we have shown the utility of microvortices in stationary droplet shear-induced by the oil phase to deconvolve the effects of cell morphology (size and stiffness) on their dynamic translational and rotational motion. The results have revealed the significant difference in cell orbital area within the microvortices in a manner dependent on oil flow rate, which presents a label-free method to detect cells with different mechanical properties. This technique will further augment the impact of droplet microfluidics for single-cell analysis and cell mechanics by enabling the simplicity of modulating the encapsulated cells with oil flow, opening new fundamental research avenues in single-cell biomechanics.

CHAPTER 4: Summary and Future Directions

This research effort will focus on incorporating the aforementioned microfluidic devices in Chapter 2 and Chapter 3 to develop platforms that are applicable to mammalian cell transfection and realizing genotype-phenotype linkage at single-cell level. Different cell model system would be selected to demonstrate the feasibility of the microfluidic platforms.

4.1   Single-cell Transfection in Droplet

Transfection efficiency is critical to the success of monoclonal antibody discovery process and production. Traditionally, Chinese hamster ovary (CHO) cells have been more difficult to transfect than HEK293 cells. For this purpose, droplet microfluidic generation device will be utilized to compartmentalize individual cell along with lipofection reagent for effective gene delivery. The Lee group has a previous publication on using micro-droplets for ten-fold increase in gene delivery, which was demonstrated by using non-adherent cell lines including K562, THP-1, and Jurkat [92]. This prior work has successfully shown a significant reduction on cell-to-cell variation in comparison to the bulk method using lipoplex-mediated intracellular delivery (Figure 4 - 1). The enhanced gene delivery in micro-droplets is attributed to the chaotic mixing inside of the droplets induced by the serpentine microchannel and co-confinement with single cells. With this aim, further optimization for higher effective gene delivery of mammalian cells will be investigated for monoclonal antibody discovery.

Specifically, the optimization of droplet transfection entails concentration of plasmid, chaotic mixing time, size of lipoplex complex, and charge ratio of lipoplex and plasmids. The cytotoxicity issue pertinent to lipoplex-mediated gene delivery presents a challenge for

prolong incubation of cells and lipoplex in droplets. Thus, cell viability in droplets with and without lipoplex transfection will be examined for the feasibility of long-term culturing. Another approach for long term culture ($\sim$72 hrs) would be utilizing hydrogel, such as alginate, agarose, or GelMA, to be incorporated in the aqueous dispersed phase. The solidification of hydrogel encapsulating with single cell and lipoplex enables an effective transfection, as well as allowing phase exchange for fresh culture media, which will be suitable for transient transfection protocol. These hydrogel droplets will be subsequently loaded into a trapping array (Figure 3 - 1) for time-resolved monitoring. Lastly, the transfection efficiency and cell viability will be evaluated by the production of fluorescent proteins and compared against bulk cell transfection. Thus, lipoplex-mediated single-cell transfection via droplet microfluidics is expected to have a broad application in gene therapy in terms of therapeutic antibody production and regenerative medicine with enhanced transfection efficiency and low cell-to-cell variation.

Optimization of transfection conditions is of paramount importance for the success of this project. In short term, parameters that were previously mentioned will be investigated to achieve optimal transfection efficiency, which is defined by the ratio of transfected cells with fluorescent expression and total number of cells after 24 to 48 hours post transfection. For long term goal of this project, a library of plasmids will be used for high throughput transient transfection to examine the production of antibodies or secretion molecules.

In addition to the need of enhancing transfection efficiency, a pool of microdroplets containing different clones of plasmid would be an attractive method for generating cell-based diversity libraries. Existing transfecting is limited to a single type of plasmid, in which scaling up transfection process with a diverse library of plasmids is cumbersome. To take

advantage of compartmentalization and high-throughput in droplet microfluidics, we propose a new method that enables transfecting single cell with a library of different plasmid in a high-throughput manner. A batch of droplets containing different clones of plasmids would be separately generated by following conventional droplet microfluidic device (Figure 4 - 2). Each unique batch of plasmid droplets are pooled together to create a plasmid library for subsequent transfection. On the other hand, cells of interest will be encapsulated in droplets on the microfluidic device from Chapter 2 with an aim to maximize single cell occupancy. These two sets of microdroplets will then be loaded using a zipper method to achieve a sequential ordering and single file, as shown in Figure 4 - 4. This droplet train will flow into a junction with abrupt expansion and constriction of channel to induce coalescence of every two droplets, which has been demonstrated in earlier publication from Dr. Abe Lee's Lab (*Figure 4 - 3*) [93]. The merged droplets will then undergo a serial winding channel to induce chaotic mixing for effective cell transfection, as shown in Figure 4 - 5. This workflow would be a proof-of-concept for single-cell transfection with a library of different plasmid in high-throughput manner. At the early stage of the project, a library of ten or less plasmids will be used for demonstrating the proof-of-concept. In terms of microfluidic chip design, the need of scaling up will be always considered for later stage. If the project is proven to be successful, this workflow can be multiplexed and automated to accommodate a larger library of plasmids, which will be beneficial for Amgen in terms of improving efficiency and shortening time to screen plasmid of interest.

To validate this proof-of-concept, a batch of droplets containing different plasmids (e.g. GFP, RFP) and lipofectin will be generated via conventional droplet generation device. The micro-droplets are very stable under the carrier oil supplemented with surfactant, which

can be stored in Eppendorf tube for months. For storing the plasmid containing droplets, the size distribution of lipoplex upon droplet generation will be evaluated using dynamic light scattering. In addition, the integrity of plasmids in droplets will be assessed by using gel electrophoresis. The suspension of mammalian cells will be encapsulated in droplets on the day of transfection. Upon merging of cell-containing and plasmid-containing droplets, the resulting droplets will be loading into droplet trapping array (Figure 3 - 4) for evaluation of transfection efficiency and time-resolved monitoring of fluorescent gene expression.

Thus, optimization of bulk lipofectamine transfection is of prime importance before incorporating into the workflow of droplet microfluidics. Transfection efficiency and cell viability were investigated by transfecting K562 cells with different dosage of lipofectamine and media. The workflow of transfection was followed by the recommended commercial protocol for Lipofectamine 3000 (ThermoFisher). The results, shown in Figure 4 - 6, demonstrated that the condition in 3% lipofectamine in culture media performed the best with 97% viability, while the cell viability was compromised in conditions with OptiMEM. Upon assessing the transfection efficiency using flow cytometry, 20% of live cells were successfully transfected in the experimental group that involved 3% lipofectamine in culture media. This suggests that the cells were lack of nutrition during the incubation. However, further optimization would be needed, such as the amount of plasmid DNA, to achieve higher transfection efficiency.
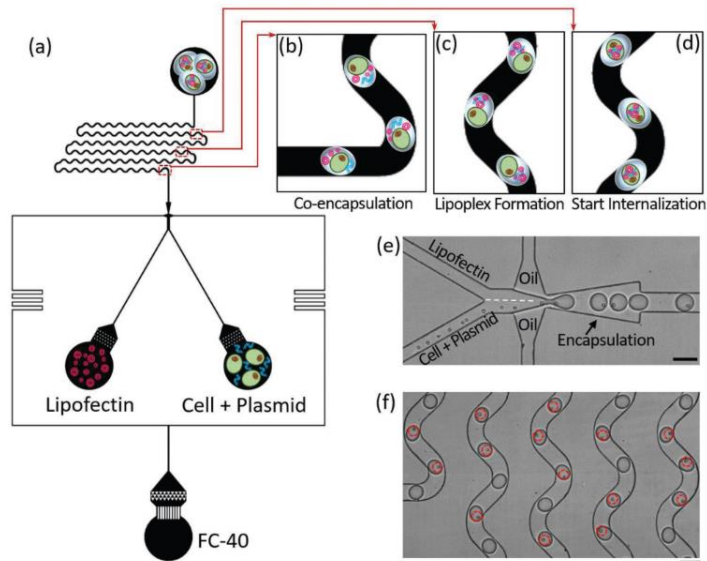
Figure 4 - 1 (a) Schematic illustration of the droplet microfluidics-based single-cell lipofection platform. (b) a single-cell is co-encapsulated with plasmids and Lipofectin. (c) negatively charged plasmids and positively charged Lipofectin self-assemble into lipoplexes during chaotic advection. (d) Entering the coencapsulated single cell by endocytosis. (e) droplet generation and the coencapsulation of single K562 cells with plasmids and Lipofectin in picoliter droplets. (f) Bright-field snapshot of droplets' chaotic advection in the winding channel. Scale bars: 100 um.
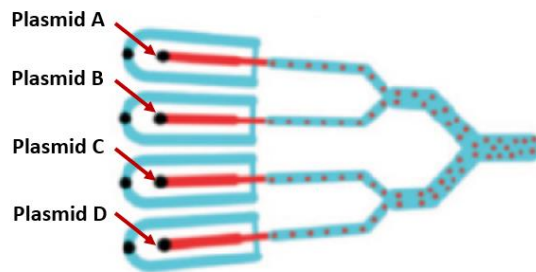
Figure 4 - 2 Schematic of plasmid library construction through droplet generation with a library of different plasmids.
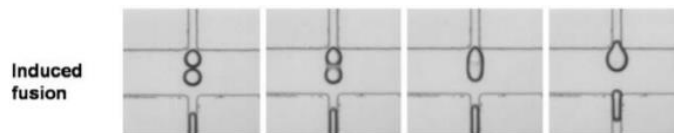
Figure 4 - 3 Serial microscopic images of sequential induced fusion. [93]

70
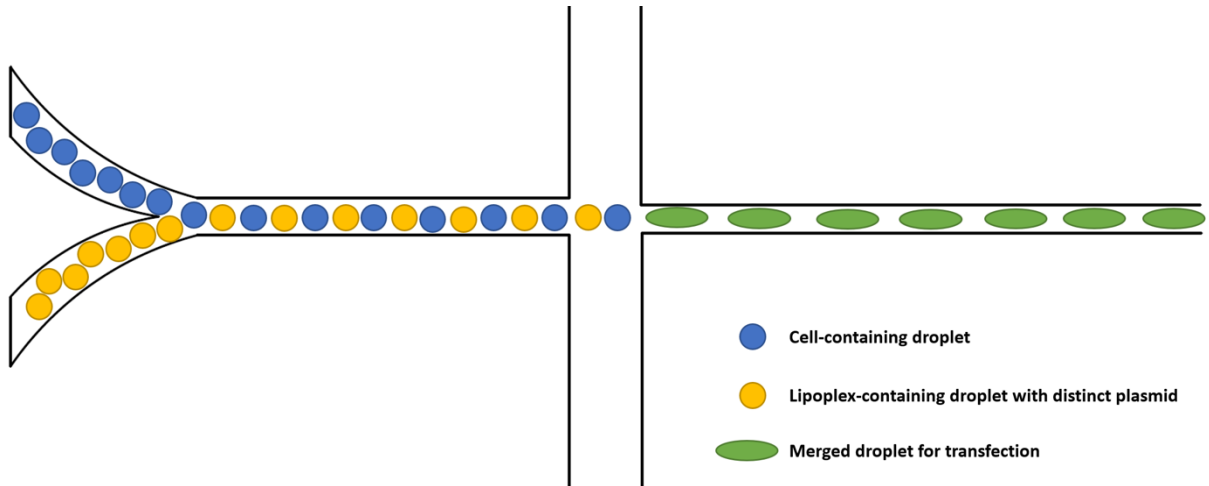
Figure 4 - 4 Schematics of the proposed approach for high-throughput single-cell transfection in droplets by coalescing cell-containing and lipoplex-plasmid-containing droplet. Two sets of close packed droplets are passively self-assembled into a sequential ordered, single file droplet train prior entering induced fusion junction.
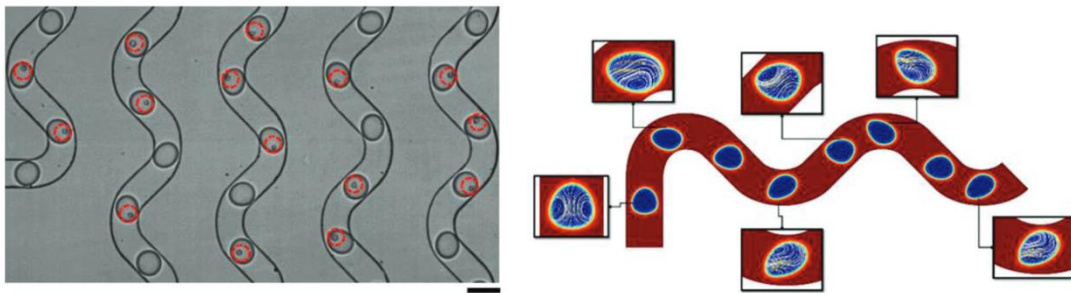
Figure 4 - 5 Coalesced droplets will immediately travel through winding channel to induce chaotic mixing for effective gene delivery into cells. Scale bars: 100 um. [92]
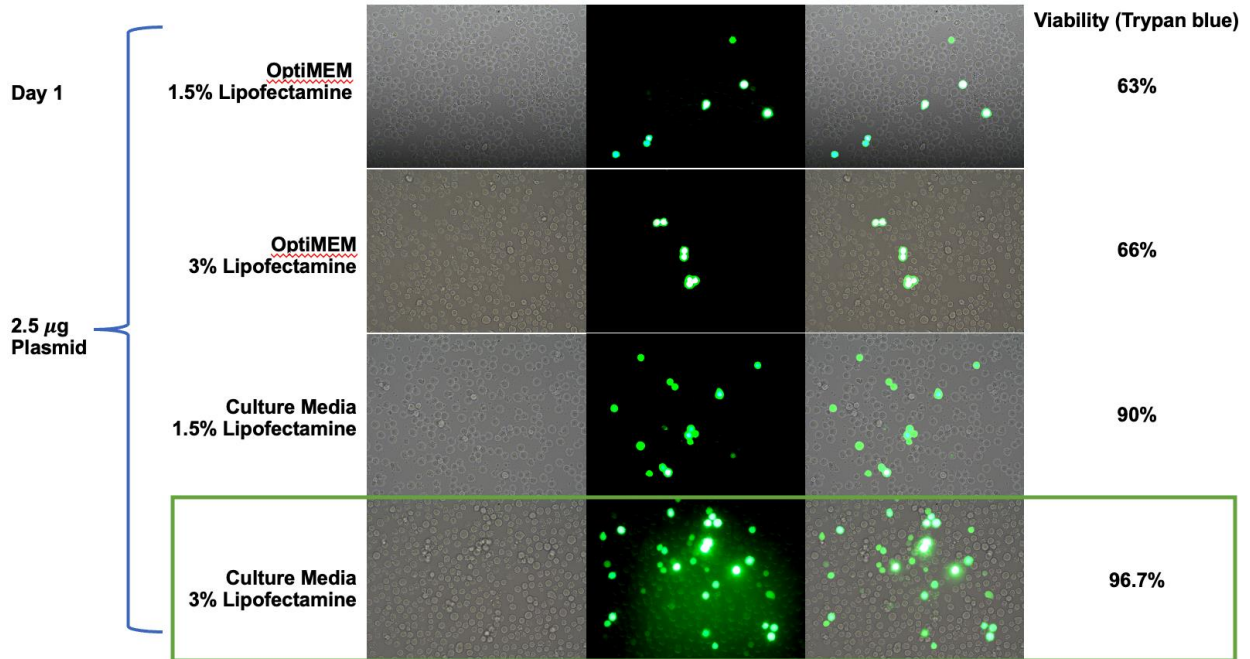
Figure 4 - 6 Optimization of chemical transfection using lipofectamine with eGFP on K562 cells.
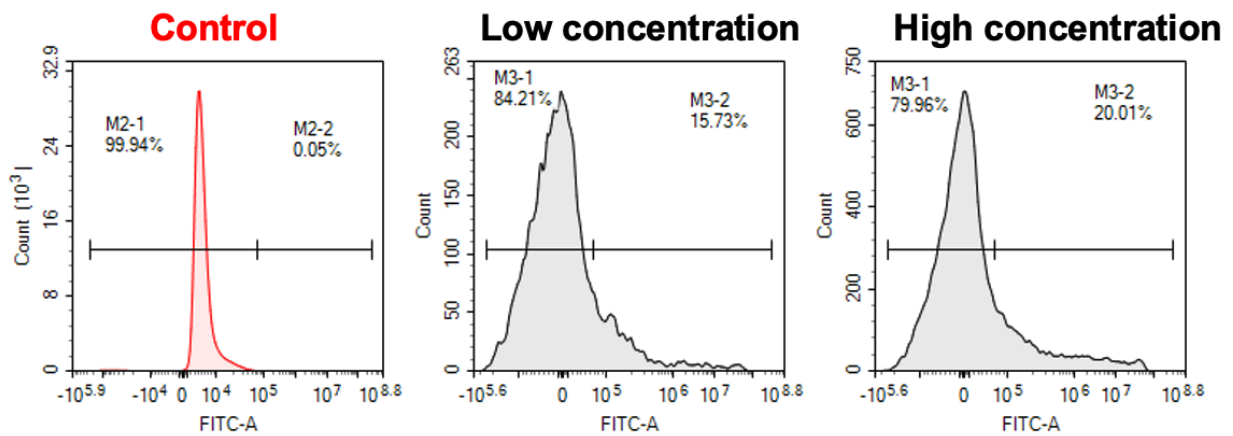
Figure 4 - 7 Flow cytometry results for bulk transfection efficiency on K562 cells by optimizing the concentration of lipofectamine.

4.2   Hydrogel Droplet Generation Optimization

To further enhance the capability of droplet microfluidic platform for downstream analysis as mentioned in Section 4.1, hydrogel droplet would be an ideal candidate for long-term culturing and dynamic temporal observation. To achieve this, we developed a hydrogel

droplet generation protocol using gelatin-methacryloyl (GelMA 80% degree of substitution). Prior loading into the droplet generating device mentioned in Chapter 2, aqueous solution containing 5% (w/v) GelMA and 0.5% (w/v) Irgacure 2959 photoinitiator was prepared by thorough mixing and incubating in water bath for 20 minutes. Subsequently, the GelMA aqueous solution and HFE 7500 oil with 2% 008-FluoroSurfactant were introduced into the droplet generation device at 4 and 5 μL/min, respectively (Figure 4 - 8). The GelMA hydrogel droplets collected in 1.5mL Eppendorf tube were exposed under ultraviolet light (long range) for a minimum of 15 minutes. The exposure to UV initiates the crosslinking of GelMA for gelation. Lastly, the droplets were retrieved for phase exchange by adding perfluorooctanol (PFO) at 1:1 ratio. Lastly, the GelMA hydrogel droplet in aqueous phase was collected and resuspend in PBS. Figure 4 - 8 illustrated the successful preliminary results for the GelMA generation and phase exchange into aqueous solution. Further optimization is required to maximize the crosslinking efficiency and minimize the exposure time for crosslinking due to its detrimental effect on cell viability.

HFE 7500 w/
2% FluoroSurfactant

GelMA Hydrogel in Oil

GelMA Hydrogel in PBS
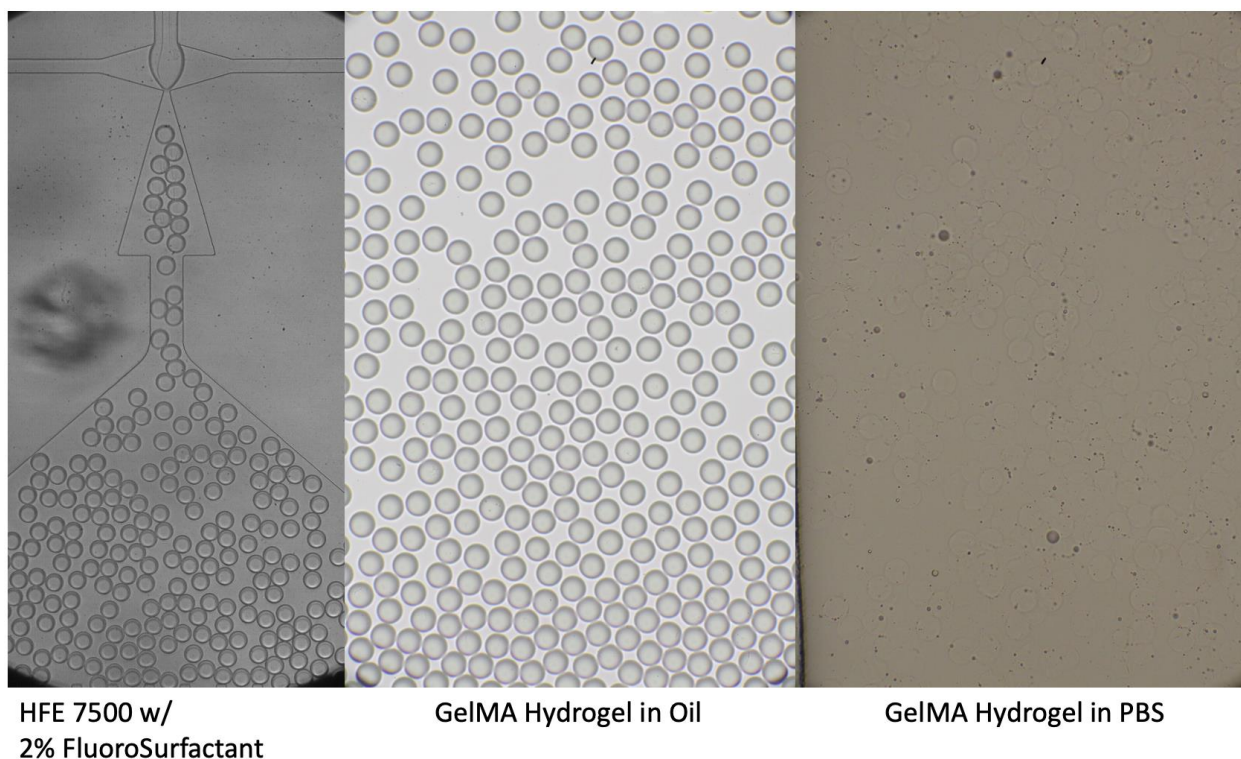
Figure 4 - 8 GelMA hydrogel droplet generation and phase exchange from oil to PBS.

4.3   Developing Cell Rotation in Droplet Device for Cellular 3D Imaging

Chapter 3 demonstrates that the microvortices in droplets can induce the encapsulated cells to exhibit either orbiting or spinning motion. Under spinning motion, we will exploit this phenomenon to precisely manipulate the rotation angle by modulating the oil flow direction, which resulting a change of rotating angle in the internal microvortices. This further advances the droplet microfluidic platform for potential microscopy application by obtaining projection view of a cell at 360 degrees. Through 3D reconstruction, we can utilize a stack of 2D projection image of a cell to reconstruct a 3D model to assess the cell topography Figure 4 - 9. To achieve this, a new droplet trapping platform is required to reduce the number of microvortices in droplet to single vortex, such that a single cell in droplet can be trapped in the center of vortex and perform spinning motion. Thus, we

propose a two-layered droplet trapping device that exploits the density difference of aqueous and oil phase for droplet immobilization. The aqueous droplets would float into the inverted microwells, where the bottom half of the droplets would be exposed to continuous flow of oil for inducing internal microvortex (Figure 4 - 10). In our preliminary results, we successfully fabricated the droplet trapping device involving inverted microwells, which demonstrated 100% droplet trapping efficiency. However, further optimization of droplet size and microwell diameters are needed to ensure single droplet occupancy per well. In addition, droplet shrinkage is also another potential risk that limits the length of experiment, which alternative materials, such as PMMA, for device fabrication is necessary to prevent sample evaporation.
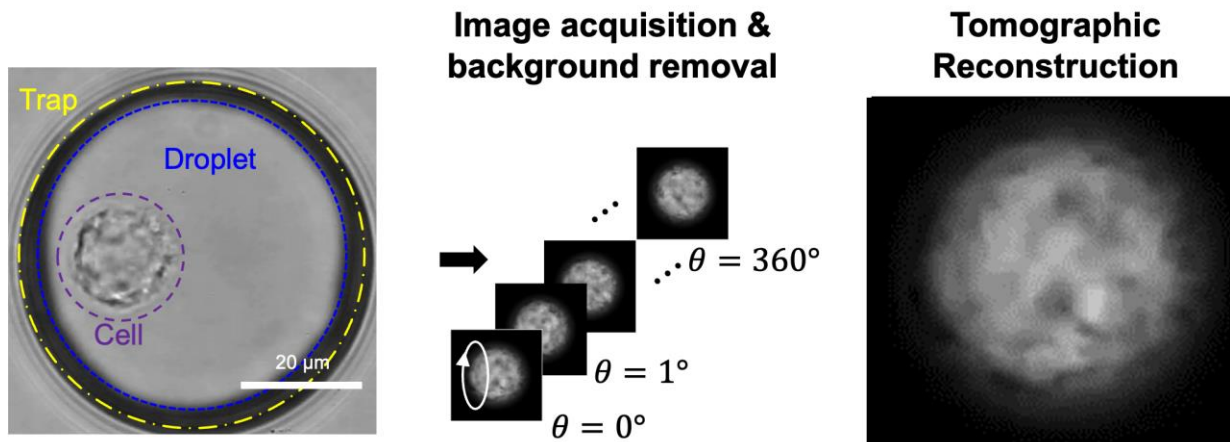
Figure 4 - 9 Schematics of droplet trapping in the inverted microwell device and 3D tomographic reconstruction through 2D projection image acquisition from a rotating cell in droplet microvortex.
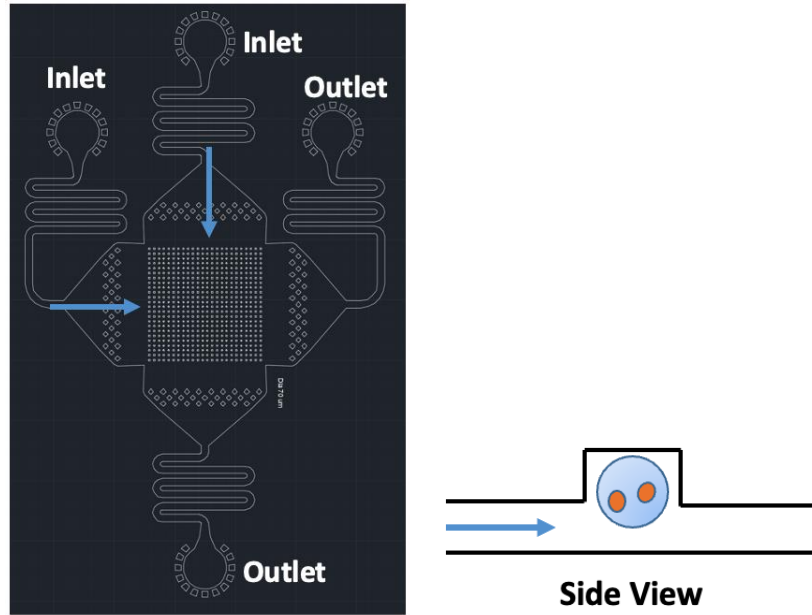
Figure 4 - 10 AutoCAD drawing of the inverted microwell device for droplet trapping.

Microwell diameter: 70μm

Microwell diameter: 40μm
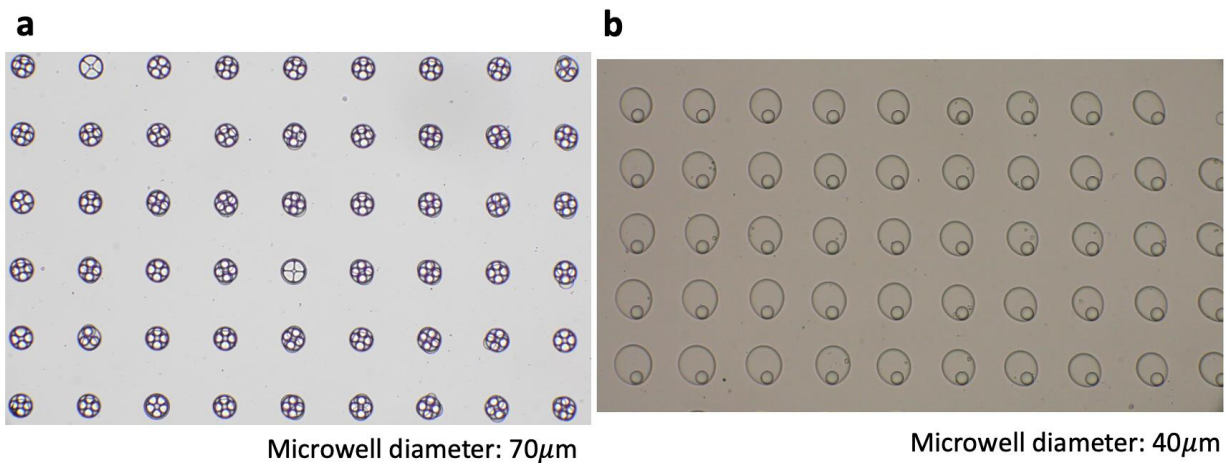
Figure 4 - 11 Droplet trapping in the microwells with diameter of a) 70 and b) 40μm, which demonstrated 100% droplet occupancy.

4.4   Conclusion

To summarize, this dissertation presented two major advancements in droplet microfluidic platforms for single-cell and cell pairing applications: 1) a 1-1-1 droplet generation device that overcomes double *Poisson* limitation for co-encapsulation of two

distinct cells in droplets, 2) a droplet trapping device that enables temporal analysis and induces microvortices in droplets for differentiating cellular morphology.

Despite several co-encapsulation techniques have been devised as mentioned in Chapter 2, the existing methods suffer from complex fabrication, lack of robustness, and selective performance depending on cell types, which limit their adaptability in many of the biological applications. Our 1-1-1 droplet generation device offers a simple setup and passive method to achieve over 2-fold improvement on co-encapsulation efficiency against double *Poisson* statistics by exploiting the hydrodynamic close packing of cells through draining the aqueous suspension of cells prior to encapsulate in droplets. In addition to the simplicity of our device, the performance of our platform is not restricted by the cell morphological properties or fluid rheology, which ensures the reliability and robustness. The improved co-encapsulation efficiency in droplets is directly beneficial to applications involving precious primary cells and cells with low density. Thus, the 1-1-1 platform demonstrated its advantages in efficient co-encapsulation, easy-of-use, passive, and robustness, which can be adapted for cell-cell interaction studies, such as natural killer cell vs. K562 tumor cell, dendritic cell vs. T cell, neural stem cell interactions, and etc.

Another major advancement made in this dissertation is the unique design of droplet trapping array, in which leading to various potential biological applications by exploiting the microvortices in droplets. Unlike the existing droplet trapping array designs, our droplet trapping array design not only efficiently immobilizes droplets for longitudinal study, but it is also capable of inducing microvortices inside the stationary droplets to dynamically modulate the movement of the encapsulated cells. This unique feature sets our design apart from the existing droplet trapping design by offering scalability, simple setup, and

unprecedented capability of cell manipulation in droplets through the control of flow rate in oil phase. In addition, we also discovered that the dynamic motion of the encapsulated cells in droplet microvortices offers a new label-free method in differentiating cell size and compliance. To the best of our knowledge, no other droplet trapping devices are capable of achieving both stationary droplets and internal microvortices in droplets. Thus, our droplet trapping platform has expanded the utility of droplet microfluidics and holds great potential for more complex single-cell applications.

As single-cell analysis holds the essential key to reveal heterogeneity in a clonal population and specific characteristics of individual cells, the demands for innovation, development, design complexity, minimizing cost, biocompatibility, and user-friendliness in droplet microfluidic technology are critical. Both 1-1-1 co-encapsulation and droplet trapping device in this dissertation overcame the technical limitations in existing droplet microfluidic technology that made it more adaptable for broader biological applications. Recent advances in artificial intelligence, pattern recognition, and machine learning and coupling with droplet microfluidics will be a powerful integration to process enormous data to decipher complex biological phenomena in bridging genotype and phenotype in single-cell resolution. Therefore, droplet microfluidics technology for single-cell and cell pairing analysis is expected to revolutionize precision medicine, drug discovery, and immunotherapy. While the author here looks forward to realizing the presented microfluidic devices in pharmaceutical and commercial settings, it is also the author's desire to inspire researchers as well as the general public regarding the importance of microfluidic technology.

REFERENCES

[1]   M. D. Slack, E. D. Martinez, L. F. Wu, and S. J. Altschuler, "Characterizing heterogeneous cellular responses to perturbations," *Proc Natl Acad Sci U S A*, vol. 105, no. 49, pp. 19306–19311, Dec. 2008, doi: 10.1073/PNAS.0807038105.

[2]   P. L. Frick, B. B. Paudel, D. R. Tyson, and V. Quaranta, "Quantifying heterogeneity and dynamics of clonal fitness in response to perturbation," *J Cell Physiol*, vol. 230, no. 7, pp. 1403–1412, Jul. 2015, doi: 10.1002/JCP.24888.

[3]   J. L. Spudich and D. E. Koshland, "Non-genetic individuality: chance in the single cell," *Nature 1976 262:5568*, vol. 262, no. 5568, pp. 467–471, 1976, doi: 10.1038/262467a0.

[4]   J. P. Junker and A. van Oudenaarden, "Every Cell Is Special: Genome-wide Studies Add a New Dimension to Single-Cell Biology," *Cell*, vol. 157, no. 1, pp. 8–11, Mar. 2014, doi: 10.1016/J.CELL.2014.02.010.

[5]   S. J. Altschuler and L. F. Wu, "Cellular Heterogeneity: Do Differences Make a Difference?," *Cell*, vol. 141, no. 4, pp. 559–563, 2010, doi: 10.1016/j.cell.2010.04.033.

[6]   J. R. Heath, A. Ribas, and P. S. Mischel, "Single-cell analysis tools for drug discovery and development," *Nat Rev Drug Discov*, vol. 15, no. 3, pp. 204–216, 2016, doi: 10.1038/nrd.2015.16.

[7]   X. Wang *et al.*, "Enhanced cell sorting and manipulation with combined optical tweezer and microfluidic chip technologies," *Lab Chip*, vol. 11, no. 21, pp. 3656–3662, Oct. 2011, doi: 10.1039/C1LC20653B.

[8]   J. T. Aerts, K. R. Louis, S. R. Crandall, G. Govindaiah, C. L. Cox, and J. v. Sweedler, "Patch clamp electrophysiology and capillary electrophoresis-mass spectrometry metabolomics for single cell characterization," *Anal Chem*, vol. 86, no. 6, pp. 3203–3208, Mar. 2014, doi: 10.1021/AC500168D/SUPPL_FILE/AC500168D_SI_001.PDF.

[9]   H. Tavakoli *et al.*, "Recent advances in microfluidic platforms for single-cell analysis in cancer biology, diagnosis and therapy," *TrAC Trends in Analytical Chemistry*, vol. 117, pp. 13–26, Aug. 2019, doi: 10.1016/J.TRAC.2019.05.010.

[10]   H. M. Davey and D. B. Kell, "Flow cytometry and cell sorting of heterogeneous microbial populations: the importance of single-cell analyses," *Microbiol Rev*, vol. 60, no. 4, pp. 641–696, Dec. 1996, doi: 10.1128/MR.60.4.641-696.1996.

[11]   A. Adan, G. Alizada, Y. Kiraz, Y. Baran, and A. Nalbant, "Flow cytometry: basic principles and applications," *https://doi.org/10.3109/07388551.2015.1128876*, vol. 37, no. 2, pp. 163–176, Feb. 2016, doi: 10.3109/07388551.2015.1128876.

[12]   S. Müller and G. Nebe-Von-Caron, "Functional single-cell analyses: flow cytometry and cell sorting of microbial populations and communities," *FEMS Microbiol Rev*, vol. 34, no. 4, pp. 554–587, Jul. 2010, doi: 10.1111/J.1574-6976.2010.00214.X.

[13]   Y. Yuan *et al.*, "Droplet encapsulation improves accuracy of immune cell cytokine capture assays," *Lab Chip*, vol. 20, no. 8, pp. 1513–1520, 2020, doi: 10.1039/c9lc01261c.

[14]   J. Briones, W. Espulgar, S. Koyama, H. Takamatsu, E. Tamiya, and M. Saito, "A design and optimization of a high throughput valve based microfluidic device for single cell compartmentalization and analysis," *Scientific Reports 2021 11:1*, vol. 11, no. 1, pp. 1–12, Jun. 2021, doi: 10.1038/s41598-021-92472-w.

[15] T. Luo, L. Fan, R. Zhu, and D. Sun, "Microfluidic Single-Cell Manipulation and Analysis: Methods and Applications," *Micromachines 2019, Vol. 10, Page 104*, vol. 10, no. 2, p. 104, Feb. 2019, doi: 10.3390/MI10020104.

[16] H. Yin and D. Marshall, "Microfluidics for single cell analysis," *Curr Opin Biotechnol*, no. 23, pp. 110–119, 2012, doi: 10.1016/j.copbio.2011.11.002.

[17] J. Seo and L. P. Lee, "Disposable integrated microfluidics with self-aligned planar microlenses," *Sens Actuators B Chem*, vol. 99, no. 2–3, pp. 615–622, May 2004, doi: 10.1016/J.SNB.2003.11.014.

[18] M. T. Guo, A. Rotem, J. A. Heyman, and D. A. Weitz, "Droplet microfluidics for high-throughput biological assays," *Lab Chip*, vol. 12, no. 12, pp. 2146–2155, May 2012, doi: 10.1039/C2LC21147E.

[19] L. Shang, Y. Cheng, and Y. Zhao, "Emerging Droplet Microfluidics," *Chem Rev*, vol. 117, no. 12, pp. 7964–8040, 2017, doi: 10.1021/acs.chemrev.6b00848.

[20] F. C. Jammes and S. J. Maerkl, "How single-cell immunology is benefiting from microfluidic technologies," *Microsyst Nanoeng*, vol. 6, no. 1, 2020, doi: 10.1038/s41378-020-0140-8.

[21] A. P. Teh, Shia-Yen; Lin, Rober; Hung, Lung-Hsin; Lee, "Droplet Microfluidics." Lab Chip, pp. 198–220, 2008. doi: 10.1039/b715524g.

[22] R. Seemann, M. Brinkmann, T. Pfohl, and S. Herminghaus, "Droplet based microfluidics," *Rep. Prog. Phys*, vol. 75, p. 16601, 2012, doi: 10.1088/0034-4885/75/1/016601.

[23] N. Shembekar, C. Chaipan, R. Utharala, and C. A. Merten, "Droplet-based microfluidics in drug discovery, transcriptomics and high-throughput molecular genetics.," *Lab Chip*, vol. 16, no. 8, pp. 1314–1331, 2016, doi: 10.1039/c6lc00249h.

[24] J. Wang *et al.*, "Droplet microfluidics for the production of microparticles and nanoparticles," *Micromachines*, vol. 8, no. 1. MDPI AG, Jan. 01, 2017. doi: 10.3390/mi8010022.

[25] A. B. Theberge *et al.*, "Microdroplets in microfluidics: An evolving platform for discoveries in chemistry and biology," *Angewandte Chemie - International Edition*, vol. 49, no. 34, pp. 5846–5868, Aug. 2010, doi: 10.1002/ANIE.200906653.

[26] A. Rakszewska, J. Tel, V. Chokkalingam, and W. T. S. Huck, "One drop at a time: Toward droplet microfluidics as a versatile tool for single-cell analysis," *NPG Asia Mater*, vol. 6, no. 10, pp. 1–11, 2014, doi: 10.1038/am.2014.86.

[27] P. Zhu and L. Wang, "Passive and active droplet generation with microfluidics: a review," *Lab Chip*, vol. 17, no. 1, pp. 34–75, 2017, doi: 10.1039/C6LC01018K.

[28] Z. Chen, J. J. Chen, and R. Fan, "Single-Cell Protein Secretion Detection and Profiling," *Annual Review of Analytical Chemistry*, vol. 12, pp. 431–449, 2019, doi: 10.1146/annurev-anchem-061318-115055.

[29] P. K. Chattopadhyay, T. M. Gierahn, M. Roederer, and J. C. Love, "Single-cell technologies for monitoring immune systems," *Nat Immunol*, vol. 15, no. 2, 2014, doi: 10.1038/ni.2796.

[30] A. K. Shalek *et al.*, "Single-cell RNA-seq reveals dynamic paracrine control of cellular variation," *Nature*, vol. 510, no. 7505, pp. 363–369, 2014, doi: 10.1038/nature13437.

[31] Q. Shi *et al.*, "Single-cell proteomic chip for profiling intracellular signaling pathways in single tumor cells," *Proceedings of the National Academy of Sciences*, vol. 109, no. 2, pp. 419–424, Jan. 2012, doi: 10.1073/pnas.1110865109.

[32] G. X. Y. Zheng *et al.*, "Massively parallel digital transcriptional profiling of single cells," *Nature Communications 2017 8:1*, vol. 8, no. 1, pp. 1–12, Jan. 2017, doi: 10.1038/ncomms14049.

[33] D. A. Lawson, K. Kessenbrock, R. T. Davis, N. Pervolarakis, and Z. Werb, "Tumour heterogeneity and metastasis at single-cell resolution," *Nat Cell Biol*, vol. 20, no. 12, pp. 1349–1360, 2018, doi: 10.1038/s41556-018-0236-7.

[34] M. Dhar, J. N. Lam, T. Walser, S. M. Dubinett, M. B. Rettig, and D. di Carlo, "Functional profiling of circulating tumor cells with an integrated vortex capture and single-cell protease activity assay," *Proceedings of the National Academy of Sciences*, vol. 115, no. 40, pp. 9986–9991, 2018, doi: 10.1073/pnas.1803884115.

[35] D. R. Bogdanowicz and H. H. Lu, "Studying cell-cell communication in co-culture," *Biotechnol J*, vol. 8, no. 4, p. 395, Apr. 2013, doi: 10.1002/BIOT.201300054.

[36] B. BL and J. IS, "Cell-cell communication in the tumor microenvironment, carcinogenesis, and anticancer treatment," *Cell Physiol Biochem*, vol. 34, no. 2, pp. 213–243, 2014, doi: 10.1159/000362978.

[37] J. M. M. den Haan, R. Arens, and M. C. van Zelm, "The activation of the adaptive immune system: Cross-talk between antigen-presenting cells, T cells and B cells," *Immunol Lett*, vol. 162, no. 2, pp. 103–112, 2014, doi: 10.1016/j.imlet.2014.10.011.

[38] T. Q. Vu, R. M. B. de Castro, and L. Qin, "Bridging the gap: microfluidic devices for short and long distance cell-cell communication," *Lab Chip*, vol. 17, no. 6, pp. 1009–1023, Mar. 2017, doi: 10.1039/c6lc01367h.

[39] M. A. Streltsova *et al.*, "Recurrent Stimulation of Natural Killer Cell Clones with K562 Expressing Membrane-Bound Interleukin-21 Affects Their Phenotype, Interferon-γ Production, and Lifespan," *International Journal of Molecular Sciences 2019, Vol. 20, Page 443*, vol. 20, no. 2, p. 443, Jan. 2019, doi: 10.3390/IJMS20020443.

[40] S. Kweon *et al.*, "Expansion of human NK cells using K562 cells expressing OX40 ligand and short exposure to IL-21," *Front Immunol*, vol. 10, no. APR, p. 879, 2019, doi: 10.3389/FIMMU.2019.00879/BIBTEX.

[41] B. Agrawal, S. J. Gendler, and B. M. Longenecker, "The biological role of mucins in cellular interactions and immune regulation: prospects for cancer immunotherapy," *Mol Med Today*, vol. 4, no. 9, pp. 397–403, Sep. 1998, doi: 10.1016/S1357-4310(98)01322-7.

[42] S. E. Shelton, H. T. Nguyen, D. A. Barbie, and R. D. Kamm, "Engineering approaches for studying immune-tumor cell interactions and immunotherapy," *iScience*, vol. 24, no. 1, p. 101985, Jan. 2021, doi: 10.1016/J.ISCI.2020.101985.

[43] C. Zalfa and S. Paust, "Natural Killer Cell Interactions With Myeloid Derived Suppressor Cells in the Tumor Microenvironment and Implications for Cancer Immunotherapy," *Front Immunol*, vol. 12, p. 565, May 2021, doi: 10.3389/FIMMU.2021.633205/BIBTEX.

[44] E. Z. Macosko *et al.*, "Highly Parallel Genome-wide Expression Profiling of Individual Cells Using Nanoliter Droplets.," *Cell*, vol. 161, no. 5, pp. 1202–1214, 2015, doi: 10.1016/j.cell.2015.05.002.

[45] L. Liu, C. K. Dalal, B. M. Heineike, and A. R. Abate, "High throughput gene expression profiling of yeast colonies with microgel-culture Drop-seq," *Lab Chip*, vol. 19, no. 10, pp. 1838–1849, 2019, doi: 10.1039/c9lc00084d.

[46] E. Brouzes *et al.*, "Droplet microfluidic technology for single-cell high-throughput screening," *Proc Natl Acad Sci U S A*, vol. 106, no. 34, pp. 14195–200, 2009, doi: 10.1073/pnas.0903542106.

[47] D. di Carlo, "Technologies for the Directed Evolution of Cell Therapies," *SLAS Technol*, vol. 24, no. 4, pp. 359–372, 2019, doi: 10.1177/2472630319834897.

[48] L. Mazutis, J. Gilbert, W. L. Ung, D. A. Weitz, A. D. Griffiths, and J. A. Heyman, "Single-cell analysis and sorting using droplet-based microfluidics," *Nat Protoc*, vol. 8, no. 5, pp. 870–891, 2013, doi: 10.1038/nprot.2013.046.

[49] N. Shembekar, H. Hu, D. Eustace, and C. A. Merten, "Single-Cell Droplet Microfluidic Screening for Antibodies Specifically Binding to Target Cells," *Cell Rep*, vol. 22, no. 8, pp. 2206–2215, 2018, doi: 10.1016/j.celrep.2018.01.071.

[50] S. Sarkar *et al.*, "Dynamic analysis of immune and cancer cell interactions at single cell level in microfluidic droplets," *Biomicrofluidics*, vol. 10, no. 5, 2016, doi: 10.1063/1.4964716.

[51] S. Sarkar *et al.*, "Dynamic analysis of human natural killer cell response at single-cell resolution in B-Cell Non-Hodgkin Lymphoma," *Front Immunol*, vol. 8, no. DEC, pp. 1–13, 2017, doi: 10.3389/fimmu.2017.01736.

[52] T. Konry, A. Golberg, and M. Yarmush, "Live single cell functional phenotyping in droplet nano-liter reactors," *Sci Rep*, vol. 3, pp. 1–5, 2013, doi: 10.1038/srep03179.

[53] T. Konry, M. Dominguez-Villar, C. Baecher-Allan, D. A. Hafler, and M. L. Yarmush, "Droplet-based microfluidic platforms for single T cell secretion analysis of IL-10 cytokine," *Biosens Bioelectron*, vol. 26, no. 5, pp. 2707–2710, 2011, doi: 10.1016/j.bios.2010.09.006.

[54] T. Konry, S. Sarkar, P. Sabhachandani, and N. Cohen, "Innovative Tools and Technology for Analysis of Single Cells and Cell–Cell Interaction," *Annu Rev Biomed Eng*, vol. 18, no. 1, pp. 259–284, 2016, doi: 10.1146/annurev-bioeng-090215-112735.

[55] D. J. Collins, T. Alan, K. Helmerson, and A. Neild, "Surface acoustic waves for on-demand production of picoliter droplets and particle encapsulation," *Lab Chip*, vol. 13, no. 16, pp. 3225–3231, Jul. 2013, doi: 10.1039/C3LC50372K.

[56] Mingyan He, J. Scott Edgar, Gavin D. M. Jeffries, Robert M. Lorenz, and J. Patrick Shelby, and D. T. Chiu*, "Selective Encapsulation of Single Cells and Subcellular Organelles into Picoliter- and Femtoliter-Volume Droplets," *Anal Chem*, vol. 77, no. 6, pp. 1539–1544, Mar. 2005, doi: 10.1021/AC0480850.

[57] A. Chen *et al.*, "On-chip magnetic separation and encapsulation of cells in droplets," *Lab Chip*, vol. 13, no. 6, pp. 1172–1181, Feb. 2013, doi: 10.1039/C2LC41201B.

[58] J. F. Edd *et al.*, "Controlled encapsulation of single-cells into monodisperse picolitre drops," *Lab Chip*, vol. 8, no. 8, pp. 1262–1264, 2008, doi: 10.1039/b805456h.

[59] K. Shahrivar and F. del Giudice, "Controlled viscoelastic particle encapsulation in microfluidic devices," *Soft Matter*, vol. 17, no. 35, pp. 8068–8077, Sep. 2021, doi: 10.1039/D1SM00941A.

[60] R. Ramji *et al.*, "Single cell kinase signaling assay using pinched flow coupled droplet microfluidics," *Biomicrofluidics*, vol. 8, no. 3, pp. 3–11, 2014, doi: 10.1063/1.4878635.

[61] K. GK and B. AS, "Field-free particle focusing in microfluidic plugs," *Biomicrofluidics*, vol. 6, no. 2, Apr. 2012, doi: 10.1063/1.3700120.

[62] X. Luo, J.-Y. Chen, M. Ataei, and A. Lee, "Microfluidic Compartmentalization Platforms for Single Cell Analysis," *Biosensors (Basel)*, vol. 12, no. 2, 2022, doi: 10.3390/bios12020058.

[63] A. K. Price and B. M. Paegel, "Discovery in Droplets," *Anal Chem*, vol. 88, no. 1, pp. 339–353, 2016, doi: 10.1021/acs.analchem.5b04139.

[64] F. Tang *et al.*, "mRNA-Seq whole-transcriptome analysis of a single cell," *Nature Methods 2009 6:5*, vol. 6, no. 5, pp. 377–382, Apr. 2009, doi: 10.1038/nmeth.1315.

[65] B. el Debs, R. Utharala, I. v. Balyasnikova, A. D. Griffiths, and C. A. Merten, "Functional single-cell hybridoma screening using droplet-based microfluidics," *Proc Natl Acad Sci U S A*, vol. 109, no. 29, pp. 11570–11575, 2012, doi: 10.1073/pnas.1204514109.

[66] A. Gérard *et al.*, "High-throughput single-cell activity-based screening and sequencing of antibodies using droplet microfluidics," *Nat Biotechnol*, vol. 38, no. 6, pp. 715–721, 2020, doi: 10.1038/s41587-020-0466-7.

[67] J. L. Madrigal *et al.*, "Characterizing cell interactions at scale with made-to-order droplet ensembles (MODEs)," *PNAS*, vol. 119, no. 5, 2022, doi: 10.1073/pnas.2110867119/-/DCSupplemental.

[68] B. Dura, M. M. Servo, R. M. Barry, H. L. Ploeghf, S. K. Dougand, and J. Voldman, "Longitudinal multiparameter assay of lymphocyte interactions from onset by microfluidic cell pairing and culture," *Proc Natl Acad Sci U S A*, vol. 113, no. 26, pp. E3599–E3608, Jun. 2016, doi: 10.1073/pnas.1515364113.

[69] J. Gole *et al.*, "Massively parallel polymerase cloning and genome sequencing of single cells using nanoliter microwells," *Nature Biotechnology 2013 31:12*, vol. 31, no. 12, pp. 1126–1132, Dec. 2013, doi: 10.1038/nbt.2720.

[70] D. H. Lee, X. Li, N. Ma, M. A. Digman, and A. P. Lee, "Rapid and label-free identification of single leukemia cells from blood in a high-density microfluidic trapping array by fluorescence lifetime imaging microscopy," *Lab Chip*, vol. 18, no. 9, pp. 1349–1358, 2018, doi: 10.1039/c7lc01301a.

[71] X. Li, Y. Tao, D. H. Lee, H. K. Wickramasinghe, and A. P. Lee, "In situ mRNA isolation from a microfluidic single-cell array using an external AFM nanoprobe," *Lab Chip*, vol. 17, no. 9, pp. 1635–1644, May 2017, doi: 10.1039/C7LC00133A.

[72] F. Abali, J. Broekmaat, A. Tibbe, R. B. M. Schasfoort, L. Zeune, and L. W. M. M. Terstappen, "A microwell array platform to print and measure biomolecules produced by single cells," *Lab Chip*, vol. 19, no. 10, pp. 1850–1859, 2019, doi: 10.1039/c9lc00100j.

[73] Y. Yoshimura, M. Tomita, F. Mizutani, and T. Yasukawa, "Cell Pairing Using Microwell Array Electrodes Based on Dielectrophoresis," *Anal Chem*, vol. 86, no. 14, pp. 6818–6822, Jul. 2014, doi: 10.1021/AC5015996.

[74] B. Dura *et al.*, "Profiling lymphocyte interactions at the single-cell level by microfluidic cell pairing," *Nature Communications 2015 6:1*, vol. 6, no. 1, pp. 1–13, Jan. 2015, doi: 10.1038/ncomms6940.

[75] X. Fu, Y. Zhang, Q. Xu, X. Sun, and F. Meng, "Recent Advances on Sorting Methods of High-Throughput Droplet-Based Microfluidics in Enzyme Directed Evolution," *Front Chem*, vol. 9, p. 168, Apr. 2021, doi: 10.3389/FCHEM.2021.666867/BIBTEX.

[76] M. Tenje, A. Fornell, M. Ohlin, and J. Nilsson, "Particle Manipulation Methods in Droplet Microfluidics," *Anal Chem*, vol. 90, no. 3, pp. 1434–1443, Feb. 2018, doi: 10.1021/acs.analchem.7b01333.

[77] P. E. Beshay, A. M. Ibrahim, S. S. Jeffrey, R. T. Howe, and Y. H. Anis, "Encapsulated cell dynamics in droplet microfluidic devices with sheath flow," *Micromachines (Basel)*, vol. 12, no. 7, Jul. 2021, doi: 10.3390/mi12070839.

[78] C. M. Leong, Y. Gai, and S. K. Y. Tang, "Internal flow in droplets within a concentrated emulsion flowing in a microchannel," *Physics of Fluids*, vol. 28, no. 11, 2016, doi: 10.1063/1.4968526.

[79] H. Song, M. R. Bringer, J. D. Tice, C. J. Gerdts, and R. F. Ismagilov, "Experimental test of scaling of mixing by chaotic advection in droplets moving through microfluidic channels," *Appl Phys Lett*, vol. 83, no. 22, pp. 4664–4666, 2003, doi: 10.1063/1.1630378.

[80] A. Huebner *et al.*, "Static microdroplet arrays: a microfluidic device for droplet trapping, incubation and release for enzymatic and cell-based assays," *Lab Chip*, vol. 9, no. 5, pp. 692–698, Mar. 2009, doi: 10.1039/B813709A.

[81] L. Labanieh, T. N. Nguyen, W. Zhao, and D. K. Kang, "Floating Droplet Array: An Ultrahigh-Throughput Device for Droplet Trapping, Real-time Analysisand Recovery," *Micromachines 2015, Vol. 6, Pages 1469-1482*, vol. 6, no. 10, pp. 1469–1482, Sep. 2015, doi: 10.3390/MI6101431.

[82] H. H. Jeong, B. Lee, S. H. Jin, S. G. Jeong, and C. S. Lee, "A highly addressable static droplet array enabling digital control of a single droplet at pico-volume resolution," *Lab Chip*, vol. 16, no. 9, pp. 1698–1707, Apr. 2016, doi: 10.1039/C6LC00212A.

[83] W. Wang, C. Yang, Y. Liu, and C. M. Li, "On-demand droplet release for droplet-based microfluidic system," *Lab Chip*, vol. 10, no. 5, pp. 559–562, Mar. 2010, doi: 10.1039/B924929J.

[84] B. B. Yellen, R. M. Erb, H. S. Son, R. Hewlin, H. Shang, and G. U. Lee, "Traveling wave magnetophoresis for high resolution chip based separations," *Lab Chip*, vol. 7, no. 12, pp. 1681–1688, Nov. 2007, doi: 10.1039/B713547E.

[85] M. Akhtar, S. van den Driesche, A. Bödecker, and M. J. Vellekoop, "Long-term storage of droplets on a chip by Parylene AF4 coating of channels," *Sens Actuators B Chem*, vol. 255, pp. 3576–3584, Feb. 2018, doi: 10.1016/J.SNB.2017.08.032.

[86] J. S. Hadamard, "Mouvement permanent lent d'une sphere liquid et visqueuse dans un liquide visqueux," *CR Hebd. Seances Acad. Sci. Paris*, vol. 152, pp. 1735–1738, 1911.

[87] K. Hamamoto, S. Ohga, S. Nomura, and K. Yasunaga, "Cellular distribution of CD63 antigen in platelets and in three megakaryocytic cell lines," *Histochem J*, vol. 26, no. 4, pp. 367–375, 1994, doi: 10.1007/BF00157770.

[88] J. J. BLUEMINK, D. LOHSE, A. PROSPERETTI, and L. VAN WIJNGAARDEN, "A sphere in a uniformly rotating or shearing flow," *J Fluid Mech*, vol. 600, pp. 201–233, 2008, doi: DOI: 10.1017/S0022112008000438.

[89] T. Neumann *et al.*, "Simultaneous 3D imaging of morphology and nanoparticle distribution in single cells with the Cell-CT™ technology," in *2008 30th Annual International Conference of the IEEE Engineering in Medicine and Biology Society*, 2008, pp. 379–381. doi: 10.1109/IEMBS.2008.4649169.

[90] L. Kelbauskas *et al.*, "Optical computed tomography for spatially isotropic four-dimensional imaging of live single cells," *Sci Adv*, vol. 3, no. 12, p. e1602580, Jul. 2017, doi: 10.1126/sciadv.1602580.

[91]   L. Huang, P. Zhao, and W. Wang, "3D cell electrorotation and imaging for measuring multiple cellular biophysical properties," *Lab Chip*, vol. 18, no. 16, pp. 2359–2368, 2018, doi: 10.1039/C8LC00407B.

[92]   X. Li, M. Aghaamoo, S. Liu, D. H. Lee, and A. P. Lee, "Lipoplex-Mediated Single-Cell Transfection via Droplet Microfluidics," *Small*, vol. 14, no. 40, pp. 1–10, 2018, doi: 10.1002/smll.201802055.

[93]   Y. C. Tan, Y. L. Ho, and A. P. Lee, "Droplet coalescence by geometrically mediated flow in microfluidic channels," *Microfluid Nanofluidics*, vol. 3, no. 4, pp. 495–499, Aug. 2007, doi: 10.1007/S10404-006-0136-1/FIGURES/4.